Fall 11-15-2017

High Power Microwave Metamaterial Based Passive and Active Devices

Hamide Seidfaraji
University of New Mexico - Main Campus

Hamide Seidfaraji
Candidate

Electrical and Computer Engineering
Department

This dissertation is approved, and it is acceptable in quality and form for publication:

Approved by the Dissertation Committee:

Christos Christodoulou , Chairperson

Edl Schamiloglu

Mark Gilmore

Anil Prinja

HIGH POWER MICROWAVE METAMATERIAL BASED PASSIVE AND ACTIVE DEVICES

by

HAMIDE SEIDFARAJI

B.Sc., Electrical Engineering,
Amirkabir University of Technology, Tehran Iran, 2005
M.Sc., Electrical Engineering,
Amirkabir University of Technology, Tehran Iran, 2008

DISSERTATION

Submitted in Partial Fulfillment of the
Requirements for the Degree of

Doctor of Philosophy
Engineering

The University of New Mexico
Albuquerque, New Mexico

December 2017

Dedication

To my Parents

Azam and Seifollah,

and To my best friend, my love, my husband

Ali

Who never stopped supporting me

ACKNOWLEDGEMENTS

I would like to thank my advisor professor, Christos Christodoulou, for accepting me as his student, giving me the opportunity to be his PhD Student. His support and guidance inspired me to work hard during my work. From him, I have learned so much.

I would like to thank our professional collaborators for their help and guidance: Prof. Edl Schamiloglu and Prof. Mark Gilmore, for all the helpful guidance and support they gave me during my PhD.

I also would like to express my gratitude to professor Mikhail Fuks, my co-author in one of the paper, for his ideas. He is a brilliant and patient mentor who would always take the time to listen to my ideas and answer my questions.

The research presented in this dissertation was supported by AFOSR MURI Grant FA9550-12-1-0489 and DARPA INVEST Grant N66001-16-1-4042.

Metamaterial Based High Power Microwave Devices

By

Hamide Seidfaraji

B.Sc., Electrical Engineering, Amirkabir University of Technology, Iran, 2005

M.Sc., Electrical Engineering, Amirkabir University of Technology, Iran, 2008

Ph.D., Electrical Engineering, University of New Mexico, Albuquerque, USA, 2017

Abstract

The goal of this dissertation is to design novel metamaterials for High Power Microwave devices. Metamaterials (MTM) are artificial periodic structures, which support reversed Cherenkov radiation and backward wave propagation. Microwave sources transform the kinetic energy of an electron beam into microwaves through the interaction of the electrons with a periodic slow wave structures (SWS). Here, a metamaterial (MTM) waveguide is proposed for use in a microwave oscillator instead of a SWS. The interaction of a multi-beam cathode with a set of MTM structures inside a cylindrical waveguide is studied and analyzed.

Group theory is used to design a metamaterial slow wave structure that uses structures with dissimilar unit cell dimensions to tune the negative permittivity and negative permeability to overlap at the same frequency. The structure is arranged azimuthally such that it can be excited using a multi-beam emitter. Using a multi-beam has some advantages. It increases the interaction with the metamaterial and therefore it enhances the output peak power (105 MW) of an BWO.

The second part of dissertation is dedicated to the design of a power combiner/splitter for THz applications. Most dangerous explosive materials, both toxic and radioactive, contain nitrogen salts with resonant absorption lines in the frequency range 0.3-10 THz. Therefore, there has been a growing interest in remotely detecting such materials by observing the spectrum of reflected signals when the suspicious material is interrogated by THz radiation. Practical portable THz sources available today generate only 20–40 mW output power. This power level is too low to interrogate suspicious material from a safe distance, especially if the material is concealed. Hence, there is a need for sources that can provide greater power in the THz spectrum. Generating and extracting high output power from THz sources is complicated and inefficient. The efficiency of vacuum electronic microwave sources is very low when scaled to the THz range and THz sources based on scaling down semiconductor laser sources have low efficiency as well, resulting in the well-known "THz gap." The reason for such low efficiencies for both source types is material losses in the THz band.

In this work an efficient power combiner is described that not only combines the THz power output from several sources, but can also form a Gaussian wave beam output. A minimum conversion efficiency of 89% with co-phased inputs in a lossy copper power combiner and maximum efficiency of 100% in a Perfect Electric Conductor (PEC)-made power combiner were achieved in simulations. Also, it is shown that the TE01 output mode is a reasonable option for THz applications since conductive losses decrease for this mode as frequency increases.

Table of Contents

List of Figures

LIST OF TABLES

Chapter 1 Metamaterial Properties

1.1 Introduction

Interest in the study of metamaterials has been increasing steadily during the last decade. Metamaterials are artificially periodic materials with quasi-periodic unit cells. Metamaterials have shown unique properties such as negative index of refraction, opposite-sign phase and group velocities and inverse Doppler effect which cannot be obtained by materials that exist in nature. They have led to several interesting applications in science and technology such as in invisible cloaking [1], [2], super lenses [3], [4], [5], terahertz spectroscopy and active metamaterial devices [6], [7], and optical applications [8]. Metamaterials have also been used in designing amplifiers, filters, and phase shifter designs [9], [10], [11], [12].

Veselago in 1960 was the first to demonstrate the feasibility of a double negative material [13].

Some metamaterials exhibit only negative permittivity (ENG), such as plasmas or metals at optical frequencies, or only negative permeability (MNG), such as magnetized ferrites. A metamaterial can be a double negative (negative permeability and negative permittivity) material (DNG) such as the one reported by Smith and his colleagues [14]. Among various kinds of metamaterials, double negative materials with simultaneously negative permittivity and permeability are the most attractive to researchers because they allow non-evanescent propagation through its medium. The various material categories are shown in Figure 0-1.

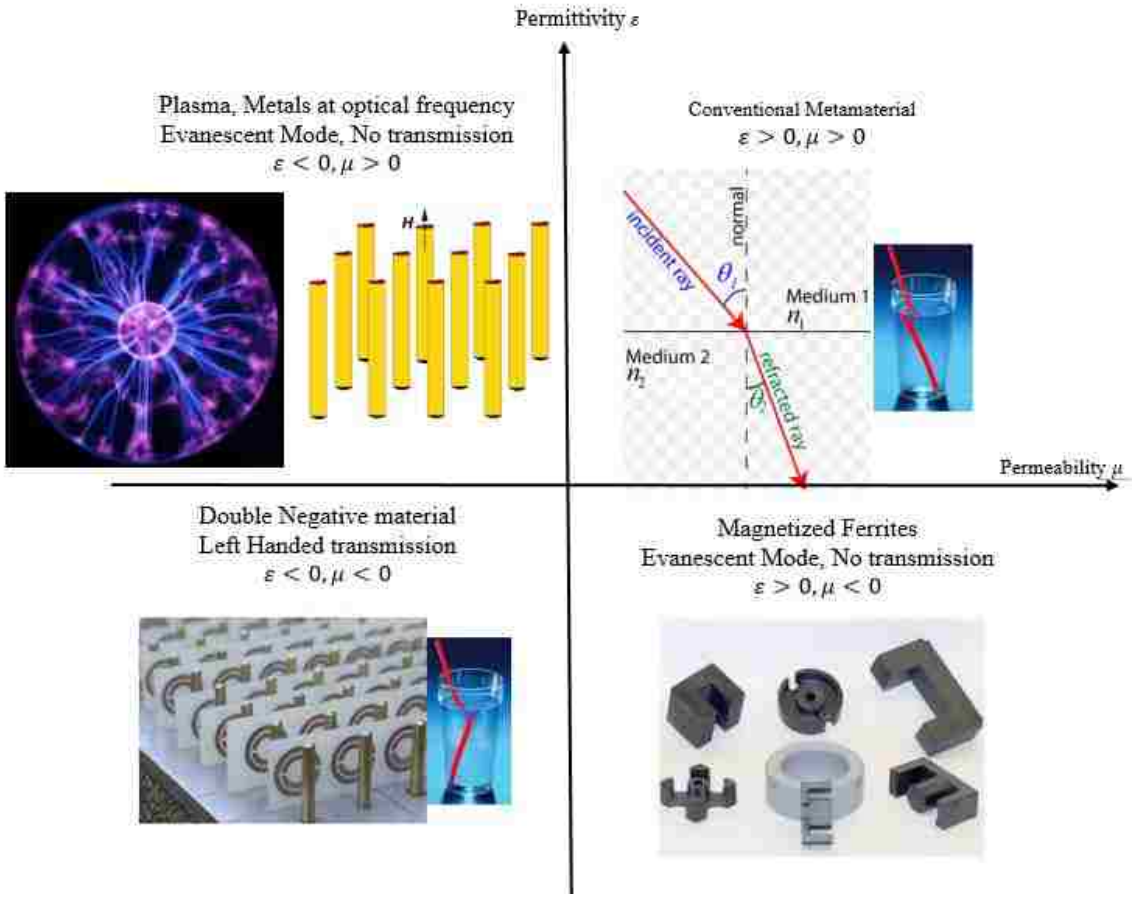

Figure 0-1 All possible combinations of permittivity and permeability.

Double negative metamaterials, are also called left-handed materials (LHM) because they form a left handed (E, H and k) where constant phase front is anti-parallel to the wave energy or Poynting vector direction.

Experimental validation of left-handed behavior was first reported in [14] [15] [16]. Before then, metamaterials were mainly an abstract mathematical concept. Pendry in [15] showed, a set of periodic metallic rods when the electric field vectors are oriented in the direction of rods, behave like plasma and the set exhibits negative permittivity below

plasma frequency. Also, Pendry showed in [17], an array of rings, and split ring resonators (SRR), behave as magnetic resonators and exhibit negative permeability.

In [16], Shelby conducted an experiment, by using metamaterial plated as a load inside a parallel plate waveguide, to show negative permeability and permittivity in the X-band frequency and left-handed propagation.

Several periodic configurations have been proposed which show negative permittivity/permeability, such as split ring resonators (SRRs) [14], electric-field-coupled resonators (ELC) [18], capacitive loaded strips (CLS) [19], metal wires [14], etc. Figure 0-2 shows some well-known examples of metamaterials unit cells.

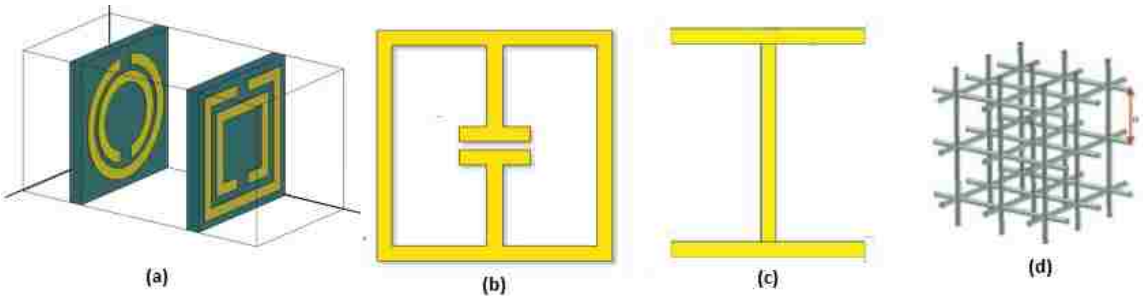

Figure 0-2 well-known Metamaterials, a) SRRs, b) ELC, c) CLS, d) Metal Rods.

Smith and his colleagues [20] showed that periodic SRRs fabricated on a dielectric substrate provide negative permeability while periodic metallic rods printed on the other side of the dielectric provide negative permittivity. Permittivity and permeability extraction method will be explained later in this chapter.

For the case of SRRs, a wave perpendicular to SRR plane, induces currents on the rings, which causes magnetic flux passing through the rings. SRRs can be modeled with as resonant LC circuits, and capacitances due to the gaps in the concentric rings.

.

1.2 Metamaterial Theory and Fundamentals

Even though metamaterials are complex structures, their electromagnetic behavior is governed by Maxwell's equations [21].

$$\nabla \times \vec{E} = -\frac{\partial \vec{B}}{\partial t} \tag{0-1}$$

$$\nabla \times \vec{H} = \vec{J} + \frac{\partial \vec{D}}{\partial t}$$

$$\nabla . \vec{D} = \rho$$

$$\nabla . \vec{B} = 0$$

where $\vec{E}$ and $\vec{H}$ are the electric and magnetic fields respectively, and $\vec{D}$ and $\vec{B}$ are the electric and magnetic flux density and $\vec{J}$ and ρ are the current and charge sources.

For a homogenous medium the constitutive parameters relate electric and magnetic fields to electric and magnetic flux through equation (0-2).

$$\vec{D} = \varepsilon \vec{E} \tag{0-2}$$

$$\vec{B} = \mu \vec{H}$$

where ε is the permittivity and μ is the permeability of the medium. The power flow (Poynting vector), can be calculated as (0-3).

$$\vec{S} = \vec{E} \times \vec{H}^{*} \tag{0-3}$$

1.2.1 Phase velocity

The phase velocity defines the velocity of constant phase front of the propagating wave. It can be defined as equation (0-4).

$$\overrightarrow{v_p} = \frac{\omega}{k}\hat{k}, \hat{k} = \frac{\vec{k}}{|\vec{k}|} \tag{0-4}$$

The phase velocity can have a value greater than the speed of light ($c = 3 \times 10^8\ m/s$) like the case of a rectangular or circular waveguide. When the waveguide is filled with a dielectric the phase velocity drops by a factor of $1/\sqrt{\varepsilon_r}$.

1.2.2 Group velocity

The group velocity defines the velocity of wave energy or the envelop of a modulated wave flowing in the direction of propagation. For a metamaterial medium, the group velocity and the phase velocity are in opposite directions and the propagation in such medium is called backward wave propagation. The group velocity is defined as equation (0-5).

$$\overrightarrow{v_g} = \frac{\partial \omega}{\partial k}\hat{s}, \hat{s} = \frac{\vec{S}}{|\vec{S}|} \tag{0-5}$$

In contrast to phase velocity, the group velocity is in direction of the Poynting vector $\vec{S}$ and $(\overrightarrow{E}, \vec{H}, \vec{S})$ always form a right-handed set of vectors in any kind of medium.

1.2.3 Left Handed Propagation

To better understand the LHM behavior, it is useful to compare the wave propagation, in RH and LH media first. In a charge-free, current-free, unbounded isotropic medium, Maxwell equations can be written as equation (0-6).

$$\vec{k} \times \vec{E}(\vec{r}) = \omega\mu(\omega)\vec{H}(\vec{r}) \tag{0-6}$$

$$\vec{k} \times \vec{H}(\vec{r}) = -\omega\varepsilon(\omega)E(\vec{r})$$

$$\vec{k} \cdot \vec{E}(\vec{r}) = 0$$

$$\vec{k} \cdot \vec{H}(\vec{r}) = 0$$

Where $\vec{k}$ is wavenumber vector and ω is the angular frequency of time harmonic fields. From equation (0-6) when ε and μ are both positive, ($\vec{E}$, $\vec{H}$,$\vec{K}$) form a right handed medium (RHM), while when ε<0 and μ<0, ($\vec{E}$, $\vec{H}$,$\vec{K}$) form a left handed medium (LHM).

1.2.4 Negative refraction

One of the interesting properties of metamaterials is its negative index of refraction. Although it may not be clear from $n^2 = \varepsilon_r \mu_r$ that double negative materials, have $n < 0$, it has been shown in [22] and also experimentally in [16], that the negative solution for n, is the only acceptable solution that satisfies the appropriate boundary conditions.

Snell's law states that,

$$n_1 \sin(\theta_i) = n_2 \sin(\theta_t) \qquad (0\text{-}7)$$

where θ_i is the angle of incident wave with normal axis and θ_t is the angle of transmitted wave with normal axis.

Figure 0-3 shows that the transmitted wave differs than that of a usual positive index material.

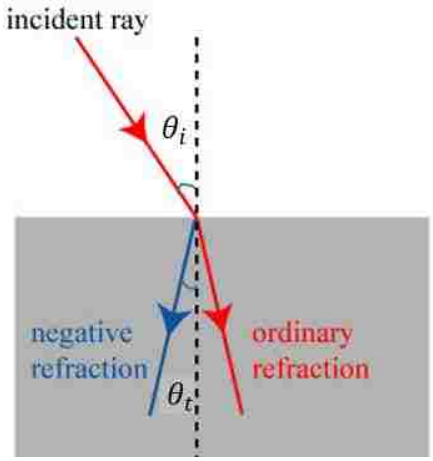

Figure 0-3 Snell's Law in negative refraction index material.

1.2.5 Inverse Doppler effect

The doppler effect states that, the frequency of a received signal is shifted as a function of relative velocity between the source and a receiver. The relative shift in frequency can be calculated through equation (0-8) [12] as:

$$\frac{\Delta f}{f_0} = n\frac{v}{c} \tag{0-8}$$

where f_0 is the frequency of the transmitted signal by the source, v is the relative velocity of the receiver to the source ($v > 0$ if the receiver moves towards the source and $v < 0$ if it is moving away). n is refraction index and c is the speed of light. It is obvious from the equation (0-8) if the receiver is moving toward the source, in a conventional material with positive refractive index, $\Delta f > 0$ and therefore, the received frequency is increased while for a metamaterial medium, $\Delta f < 0$ and the received signal has a lower frequency than f_0.

1.2.6 Dispersive LHM

Double negative materials are always dispersive. The energy density of a dispersive medium can be written as equation (0-9) [23] as:

$$W = W_e + W_m = \frac{\partial(\omega\varepsilon)}{\partial\omega}E^2 + \frac{\partial(\omega\mu)}{\partial\omega}H^2 \tag{0-9}$$

In a non-dispersive medium the stored energy density simplifies to equation (0-10).

$$W = W_e + W_m = \varepsilon E^2 + \mu H^2 \tag{0-10}$$

For LHMs with $\varepsilon < 0$ and $\mu < 0$ equation (0-10) is not valid because the electric and magnetic energy cannot have negative values.

According to the law of entropy, stored energy density has a positive value, so $\frac{\partial(\omega\varepsilon)}{\partial\omega} > 0 \; and \; \frac{\partial(\omega\mu)}{\partial\omega} > 0$ which proves that a double negative medium is always a dispersive medium.

1.3 Metamaterial Constitutive Electromagnetic parameter retrieval

Metamaterials are inhomogeneous periodic structures and for inhomogeneous media it is a complicated procedure to use the Maxwell equation directly. For a metamaterial the details of local electromagnetic solution inside the structure lattice are unimportant, but the average effect of the lattice is more of interest, and hence the local fields are averaged and the macroscopic form of the values are the ones used in Maxwell equations. This procedure is called homogenization procedure [20]. Therefore, defining effective ε and μ for an inhomogeneous medium is important.

The Drude-Lorentz model can be used to write the constitutive parameters of any medium as:

$$\varepsilon(\omega) = 1 - \frac{\omega_p^2 - \omega_{0e}^2}{\omega(\omega + j\Gamma_e) - \omega_{0e}^2} \tag{0-11}$$

$$\mu(\omega) = 1 - \frac{F\omega^2}{\omega(\omega + j\Gamma_m) - \omega_{0m}^2}$$

Where ω_p is the plasma frequency, ω_0 is the resonant frequency and Γ is the damping factor caused by material loss. The term "e" and "m" refer to electric and magnetic respectively and F is the filling ratio factor of the metamaterial. Filling factor ratio shows volume of the scattering material to its total physical volume.

Different Methods for extracting the effective constitutive parameters of an inhomogeneous medium have been reported [20], [24], [25]. In general, these methods also

make use of the reflection and transmission coefficients (scattering parameters) to calculate the metamaterial effective constitutive parameters. The scattering parameters of any periodic structure, can be simulated using a full wave solver such as CST. Smith in [20], modeled the metamaterial with a homogenous slab of width d, a refractive index n and an impedance Z, to show that equation (0-12) can be used to calculate the effective constitutive parameters of a metamaterial slab model.

$$n = \frac{1}{kd}\cos^{-1}\left[\frac{1}{2S_{21}}(1 - S_{11}^2 + S_{21}^2)\right] \tag{0-12}$$

$$Z = \sqrt{\frac{(1 + S_{11})^2 - S_{21}^2}{(1 - S_{11})^2 - S_{21}^2}}$$

$$\varepsilon = \frac{n}{Z}$$

$$\mu = nZ$$

However, the extraction method proposed by Smith result in unstable results for all-metallic thick complementary structures. Moreover, because $\cos^{-1} function$, has several branches as the solution, Smith's method suffers from not being able to determine unique values for the effective constitutive parameters.

Zsolt Szabó and his colleagues in [24] proposed an improved algorithm to calculate effective constitutive parameters of a metamaterial. They used Kramers–Kronig relations to yield a unique solution. The method showed that accurate results can be provided for the refractive index when it involves more than one branch of the complex logarithmic function. However, the method still suffers from instability results for thick or all-metallic complementary structures.

In [25], an explicit approach for the electromagnetic parameter retrieval of a metamaterial was proposed. The proposed approach determines the unique constitutive parameters of a metamaterial using a stepwise method. The stepwise approach retrieves accurate stable electromagnetic parameters even for thick metamaterials. It also retrieves the magneto-electric coupling coefficients of the metamaterial in the case that structure exhibit bianisotropic behavior. For this dissertation, the stepwise method has been used for EM metamaterial parameter retrieval. From [25], a metamaterial unit cell with periodicity d in the direction of propagation is shown in Figure 0-4.

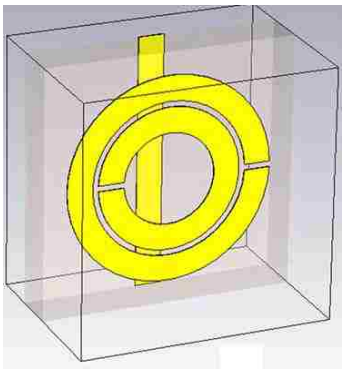

Figure 0-4 Bianisotropic composite unit cell [25].

Its effective refractive index, n, μ_y as effective permeability of the metamaterial, ε_z as the effective permittivity of metamaterial, and ξ_0 as the effective magneto-electric coupling coefficient are given by the following equations:

$$n = \frac{[Im(\ln(T) \mp 2m\pi - iRe(\ln(T))}{k_0 d} \tag{0-13}$$

where

$$T = \frac{\Gamma_1(1-\Gamma_1\Gamma_2)S_{21}}{(1-\Gamma_1\Gamma_2)(\Gamma_1 - S_{11}\Gamma_1\Gamma_2)} \tag{0-14}$$

$$\Gamma_1 = \frac{z_{w1} - 1}{z_{w1} + 1}, \Gamma_2 = \frac{z_{w2} - 1}{z_{w2} + 1}$$

$$z_{w1} = \frac{\mu_y}{n + i\xi_0}, z_{w2} = \frac{\mu_y}{n - i\xi_0}$$

$$\xi_0 = \frac{n(\Gamma_2 - \Gamma_1)}{i(1 - \Gamma_1\Gamma_2)}$$

$$\mu_y = \frac{(1 - \Gamma_1\Gamma_2)(n^2 + \xi_0^2)}{n(1 + \Gamma_1\Gamma_2) - 2n\Gamma_1 - i\xi_0(1 - \Gamma_1\Gamma_2)}$$

$$\varepsilon_z = \frac{n^2 + \xi_0^2}{\mu_y}$$

As it can be seen from equation (0-13), the n value, is a function of branch number m. The stepwise technique, proposes a recursive technique to choose the correct branch m and to avoid the ambiguity problem in the defining refractive index n. More details about the stepwise technique can be found in [25].

1.4 Conventional and Complementary Metamaterial Structures

The most well-known metamaterial unit cell structure is the split ring resonators (SRR). Basically, split ring resonators are made of a pair of annular rings, with the same center printed on a dialectric substrate. There is a gap in each ring printed 180 degrees out of phase as shown in Figure 0-5.

Here the constitutive parameter retrieval of the well-known simultaneously double negative material proposed in [14] is presented. In this particular case, the copper thickness of the square printed rings and rod is 0.017mm, the linewidth of each ring is w = 0.14 mm, the width of the rod is 0.14mm, the outer ring length, is l = 2.2 mm, the gap in the rings is g = 0.3mm, the gap between outer and inner ring is 0.15 mm, and the substrate is FR4

($\varepsilon_r = 4.4\ and\ loss = 0.02$) with 0.25mm thickness [20]. The structure unit cell is shown in Figure 0-5.

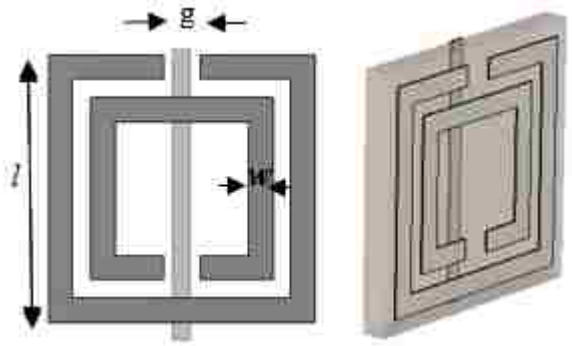

Figure 0-5 Simultaneously Double negative metamaterial.

The retrieved effective constitutive parameters using the step-wise technique [25] are shown in Figure 0-6. It is clear from Figure 0-6 that for frequencies below the resonant frequency the real part of magnetic permeability of SRR becomes large (positive) and goes to negative values at frequencies above than the resonant one.

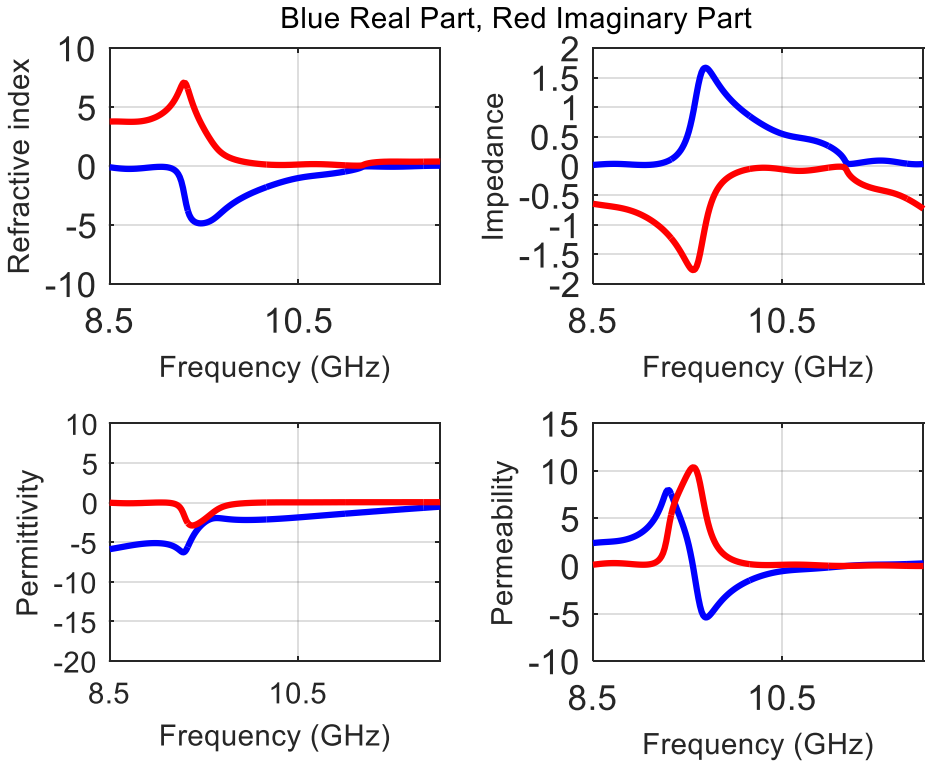

Figure 0-6 Effective refraction index, Impedance, permittivity and permeability of metamaterial of Figure 0-5.

1.5 Equivalent circuit of metamaterial

In this section, a brief review of equivalent circuits of metamaterials is presented. Next, a genetic algorithm approach is presented to extract equivalent circuit parameters of any microwave device based on its scattering parameters. The technique can be used either for finding the equivalent circuit of a unit cell or equivalent circuits of periodic structures in general. It can be shown that even an infinite periodic metamaterial structure can be modeled using ladder circuits but with finite steps that can lead to acceptable accuracy.

To implement some HPM passive devices such as phase shifters, having equivalent circuits of different microwave elements such as stubs, irises, SRRs, etc. is important. These equivalent circuits, first help predict metamaterial behavior and resonance frequency, and second, help determine the geometrical parameters that can be used to construct a specific metamaterial.

In [12] equivalent circuits of metamaterials have been discussed in detail. However, the equivalent circuits proposed were analytical models valid only for specific metamaterial unit cells. For example, the equations presented in [12] to find inductance and capacitance of a circular SRR, but only valid for split ring resonators. Thus, when it comes to complicated metamaterial unit cells, these analytical formulations fail and cannot be used to deal with more complex unit cells. Also, in the proposed equivalent circuit, the metamaterial is replaced by a simple parallel LC model since the metamaterial unit cells are resonant structures that behave like tank circuits. Substituting a metamaterial with a simple parallel LC circuit does not account for all of the metamaterial properties. The equivalent circuit can just predict the resonance frequency but the actual metamaterial behavior over a certain range of frequencies is not modeled. In addition to that, the

equivalent circuits do not even take the coupling between unit cells into account. Finally, the proposed equivalent circuit models fail for medaling complicated structures.

1.5.1 Genetic Algorithm

In genetic algorithms, a population of candidate solutions to a problem is evolved toward better solutions. Each candidate solution has a set of properties which is improved through an algorithm. The evolution usually starts from a population of randomly generated individuals with random properties. In each iteration (generation), the fitness of every individual in each generation is evaluated; the fitness of each individual is the value of the goal function in the problem which needs to be maximized or minimized. The best individuals from their fitness value point of view are stochastically selected from the current population, and each individual's properties which were selected randomly in the first iteration, are modified to form a new generation. The new generation of candidate solutions is then used in the next iteration of the algorithm. The algorithm stops when an acceptable fitness level has been reached for the population [26].

1.5.2 Metamaterial Equivalent Circuit Using Genetic Algorithm

In this work, it is shown that genetic algorithms can be used to come up with a precise equivalent model of any microwave circuit over any frequency range. Machine learning techniques, such as neural networks, and genetic algorithms, can be used to determine equivalent circuits of complicated microwave devices since they can predict more than one resonance if the microwave device is a multi-resonance device.

In the proposed genetic algorithm model, first a unit cell consisting of inductors and capacitors, like the one shown in Figure 0-7 is considered.

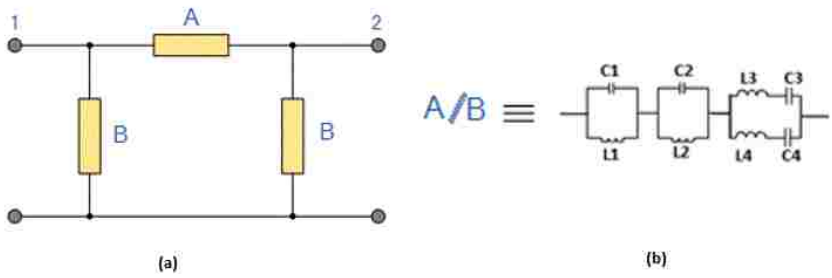

Figure 0-7 Unit cell model of proposed equivalent circuit.

The values for $\{L_1, L_2, L_3, L_4, C_1, C_2, C_3, C_4\}$ will change through for various genes. The final equivalent circuit implementation of a microwave element/device using a genetic algorithm is explained in the following steps:

Initial population: Each individual (solution) includes 16 variables as L1, L2, L3, L4, L5, L6, L7, L8, C1, C2, C3, C4, C5, C6, C7, and C8. Eight of them correspond to "A" impedances and the other eight represents to "B" impedances.

Fitness function or goal function: The fitness of each individual equivalent circuit set describes how well the scattering parameters of the corresponding two port equivalent circuit fits the scattering parameter of microwave elements (such as a metamaterial structure) obtained from CST simulation. In the implementation, the mean squared error (MSE) of the scattering parameter differences has been used as the fitness function and is defined as equation (0-15).

$$\text{MSE2} = \sum_{i=1}^{n} \left| S21_{CST} - S21_{Eqv} \right| \qquad \text{(0-15)}$$

$$\text{MSE1} = \sum_{i=1}^{n} \left| S11_{CST} - S11_{Eqv} \right|$$

$$\text{MSE} = \min(MSE1, MSE2) = \text{fitness}$$

For the split ring resonator, presented in Figure 0-5, from [20], the genetic algorithm equivalent circuit approach results in the following circuit and the following frequency properties, shown in Figure 1-8.

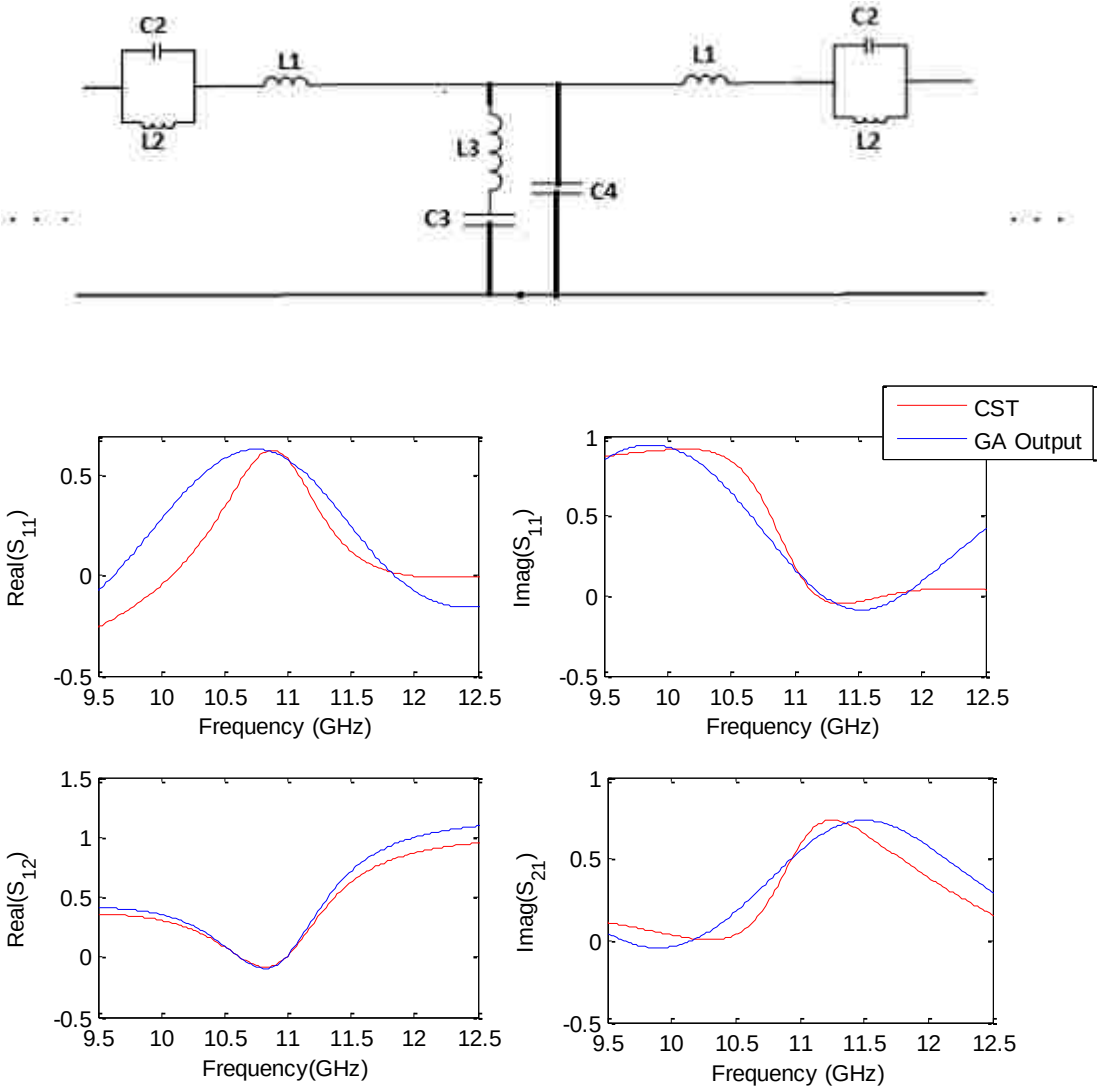

Figure 0-8 Scattering parameter of GA optimization and CST S-parameters.

2 Chapter 2 Backward Wave Oscillators

2.1 Introduction

Depending on the HPM application, the desired output power and frequency of operation, there are various sources that can be used. Most of these sources are based on vacuum electronics [27]. In this work, the interest is in metamaterial based vacuum electronic devices which generate power from electron beams in the S-band microwave frequency range. More specifically, the focus is on backward wave oscillators (BWOs) and travelling wave tube (TWTs) whose basic operation principles will be discussed in this chapter.

2.2 Backward Cherenkov Radiation

Cherenkov radiation states that when a charged particle moves faster than the phase velocity of a medium, it will radiate [28], [29]. The Cherenkov radiation effect can be explained through the conservation of energy and momentum which is beyond the scope of this work.

Backward Cherenkov radiation that happens in a double negative metamaterial medium has been validated experimentally in [30] and is of interest in this work. The radiated wave from a relativistic electron charge has a spherical waveform which propagates in a Cherenkov cone envelope as shown in Figure 2-1. Depending on the medium EM constitutive properties, if the medium of wave propagation is a positive index medium then the wave fronts propagate in forward direction like Figure 2-1(a) whereas in a negative refractive index medium the wave is a backward wave, called backward Cherenkov radiated wave, shown in Figure 2-1(b).

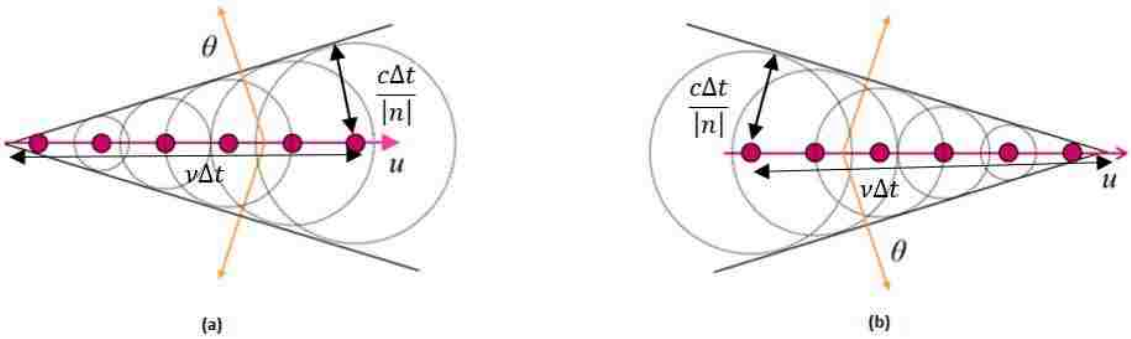

Figure 2-1 Cherenkov shock waves in a material a) positive refraction index b) negative refraction. index

The angle between the particle velocity direction and the wave front (radiation direction and the velocity of the particle direction), is calculated through equation (2-1).

$$\cos(\theta) = \frac{c}{nv} \tag{2-1}$$

Where c is the speed of light, n is the material index and v is the relativistic charge velocity. Spherical wavefronts propagate away from a particle with a phase velocity of $c/|n|$ which is faster than the speed of light [31]. The wavenumber of the generated Cherenkov wave is calculated by equation (2-2) as:

$$k_z = \frac{\omega}{c} n \cos(\theta) \tag{2-2}$$

2.3 Principles of operation for BWOs and TWTs

Travelling-wave tubes (TWTs) and Backward Wave Oscillators (BWO) are microwave amplifiers and oscillators respectively. In these devices, electron beams are interacting with electromagnetics (EM) fields and generate RF power. In Figure 2-2 a schematic of a BWO is shown. The basic components of a BWO are an electron gun to send electron beam, a slow wave structure, a collector to dump electrons as the beam passes through the structure, and a solenoid to provide a static magnetic field. One of the basic components of a BWO/TWT is the static magnetic field. The static magnetic field (B_0) is

the only DC field in BWO/TWT which is parallel to the electron beam and confines electron beams movement in the axial direction and minimizes the azimuthal motion of electrons.

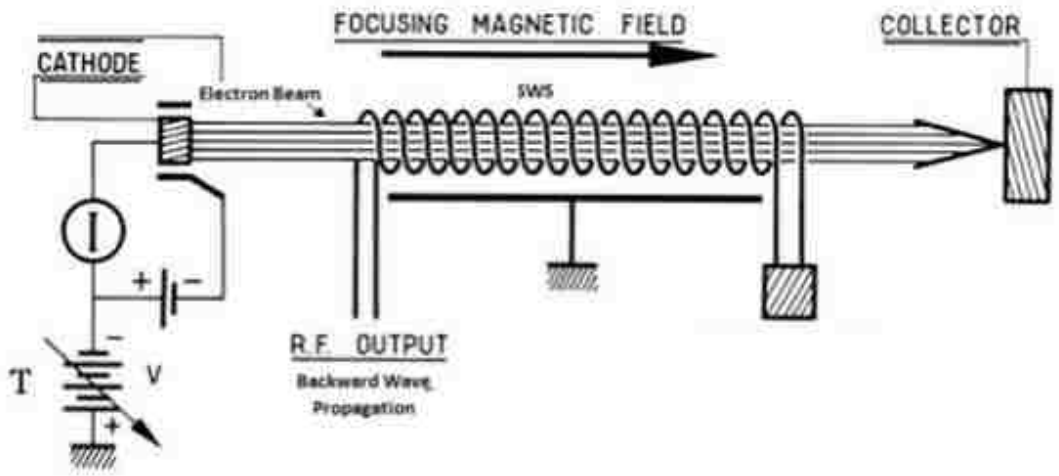

Figure 2-2 Backward wave oscillator schematic.

As it can be seen from Figure 2-2, the BWO/TWT devices have a slow wave structure inside their enclosure to slow down the phase velocity of the wave and keep it in synchronism with the electron velocity. So, this device function is based on the Smith-Purcell radiation principles [32]. The first TWT was built by Rudolph Kompfner in 1943 [32].

When an electron beam moves inside the slow wave structure, with the EM phase velocity less than the speed of light, the electron beam interacts with the slow electromagnetic wave. If the electron beam velocity is in synchronized with the SWS phase velocity, the electron beam gets modulated, then the electron beam forms bunches and thus Cherenkov radiation occurs.

TWTs and BWOs usually interact with TM modes, since a TM mode provides an axial electric field E_z which creates electron bunches. The difference between a TWT and a BWO is the input RF signal. A TWT is an amplifier which has an input RF signal

amplified through Cherenkov radiation radiated by electron beam bunches, while a BWO is an oscillator without input signal. The signal is generated from electron noise.

Like all types of oscillators, a BWO mechanism is based on instability. Instability in BWO comes from noise in the electron beam, (the frequency spectrum of the noise is very wide). So BWOs do not need any input microwave signal.

2.3.1 Mechanism of electron bunching

John Pierce was the first to explain the theory, principals and mechanism of slow wave structure devices in [33]. Pierce showed when a DC electron beam is confined by magnetic field and axially passing through a slow wave structure, it interacts with axial electric component of TM mode in the structure if TM mode wave phase velocity inside structure value is approximately equal to electron beam velocity.

To understand electron bunching, as it has been shown in Figure 2-3, at first EM wave and electron beam have the same velocity and their relative velocity is zero. Therefore, the TM wave and the electron beam are stationary. To explain this better, the frame of reference is set where both EM wave and electron beam are stationary and do not move. Since $v_{ph} \approx v_{beam}$ a stationary reference is valid for both. At first, electrons enter the BWO with uniformly distributed phase and therefore, fill all the wave phases uniformly [34]. According to equation (2-3) and (2-4) As time passes, some of electrons accelerate (those that experience negative half of electric filed period) and some of them decelerate (those electrons interact with positive electric field)

$$\vec{F} = m\vec{a} = \vec{E}q \tag{2-3}$$

Therefore

$$\frac{d\vec{v}}{dt} = q\frac{\vec{E}}{m} \tag{2-4}$$

Where m is electron mass and E is axial component of electric field (TM mode).

The accelerating or decelerating results from the AC electric field, form bunches. After sufficient time, in long enough distance from the entry point, electrons form a sequence of repeated electron bunches around the points where the electric field crosses zero as shown in Figure 2-3. Now one can see why the most coherent bunching happens when $v_{ph} = v_{beam}$

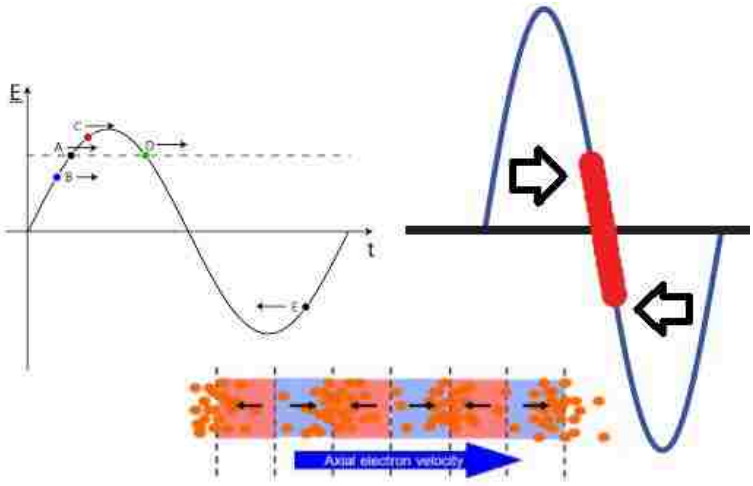

Figure 2-3 Electron bunching in Slow wave structure when electron velocity is close to electric field velocity (stationary).

However, since the electron bunches form at the zero electric field point, the energy cannot be extracted from them practically. To be able to extract RF energy from the electron bunches, the electron bunches should form on non-zero filed points. So, in practice, $v_{beam} > v_{ph} (\approx v_{beam})$ in order shift the electron bunches form zero electric point.

It is know that a charged particle with time-changing momentum radiates. When a particle starts to accelerate, depending on the acceleration direction and value, a time

varying electric field will be generated. From Maxwell's l equations, this time changing electric field, generates a magnetic field component and radiation starts.

Hence, in Figure 2-3 each accelerated electron in the electron bunch starts to surrender its energy to the generating RF wave. After some time, electrons bunches that have given an important amount of their energy to the RF signal, enterthe accelerating electric field region and begin to take back RF energy form the RF signal and output power generation stops growing, which is called saturation.

To avoid such phenomena, electron bunches must not travel more than half a wavelength, and the BWO length need to be terminated after the time electrons form bunches and give the maximum possible energy to RF signal generation [34].

As explained before, to make electron beam-RF field interaction possible and satisfy the condition $v_{ph} \approx v_{beam}$, the BWO/TWT structure should support "slow" wave propagation, i.e. slow wave propagation with phase velocity less than speed of light. There are different kinds of slow wave structures such as a metal helix [32], a corrugated waveguide [35], and metamaterials [36]. In this work, metamaterials are used to provide slow wave propagation medium inside the BWO. It has been shown that for a BWO to satisfy the interaction, the group velocity and phase velocity of the slow wave structure need to be of the opposite sign [36]. This is the one of metamaterials characteristics discussed in chapter 1, so metamaterials are a suitable candidate to be used as the slow wave structure.

2.3.2 Start Current for Oscillation

BWOs generate RF output with zero input signal. However, for oscillation to start, the beam current should be greater than start current (I_{st}). The start current is a key factor

and it is a function of mode of operation, electron beam energy and BWO length [34]. Start current can be calculated through equation (2-5).

$$I_{st} = 4U_0 \frac{(CN)_{st}^3}{ZN^3} \tag{2-5}$$

U_0 is beam energy, N shows the length of structure in wavelength, $N = L/\lambda_z$ which $\lambda_z$is the wavelength, L is the total length of BWO, and C is the Pierce parameter calculated by equation (2-6).

$$C^3 = \frac{I_0 K}{4U_0} \tag{2-6}$$

Where I_0 is the electron beam current. Z is the interaction impedance of structure, and I_0 is beam current. Using [34], $(CN)_{st}$ is 0.314 for TM_{01} mode.

Generally, the beam current is chosen as $2 \times I_{st} < I_{beam} < 7 \times I_{st}$ for a BWO. For Optimal BWO operation the beam current is 2-3 times the start current. If beam currents go as high as 7 or more then we are in the cross-excitation instability regime, Equation (2-5) gives a rough estimation of the start current and a more accurate value for a BWO with specific slow wave structure, can be found trough PIC simulation [37].

2.3.3 Dispersion Engineering

If electromagnetic waves with different wavelengths propagate with different velocities in one circuit/medium, the medium is called dispersive. The $\omega - \beta$, diagram, is used to explain the dispersive property of a medium [38]. For example, for a rectangular waveguide (WR-90), working in X-band, the dispersion diagram is shown in Figure 2-4 which is asymptotic to the light line for all modes.

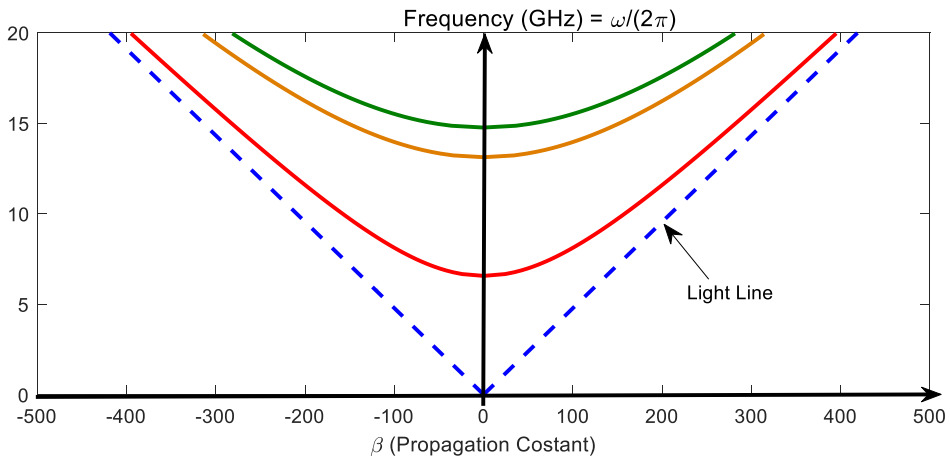

Figure 2-4 Dispersion diagram of a smooth-walled WR-90 waveguide ($TE_{10}(red), TE_{20}(green)\ and\ TE_{01}(golden)\ mode$).

2.4 Floquet's Theorem

In slow wave structures vacuum devices such as BWOs, electron beam-EM wave interaction is achieved by loading a waveguide carrying EM wave with periodic loads (corrugations). The role of corrugation is to decrease the phase velocity of spatial harmonics to a value less than the speed of light and equal to the speed of electrons. Therefore, as explained in section 2.3.1 strong electron bunching forms. Periodic structures, cause several periodic reflections due to the presence of corrugations, which lead to an infinite spectrum of harmonics that propagate with a phase velocity slower than the speed of light. Periodic loads may have the form of a helix, rods, iris or metamaterials [39].

Assume the EM field in a medium has the form of equation (2-7).

$$E(r,t) = E(x,y,z)e^{i\omega t} \tag{2-7}$$

If the structure is periodic in the z direction, with period P, the magnitude of the electric and magnetic field components also need to be periodic with period P as indicated in equation (2-8).

$$E(x, y, z + P) = E(x, y, z)e^{-i\varphi} \tag{2-8}$$

If the wave is propagating in z direction, $E(x, y, z) = E(x, y)e^{-ik_z z}$, having equation (2-8), phase shift is calculated as $\varphi = k_z P$.

2.4.1 Spatial harmonics

Having a periodicity P, the electric field cab be written in the form of a Fourier series as equation (2-9).

$$E(x, y, z, t) = \sum_{n=-\infty}^{n=\infty} E_n(x, y)e^{(i\omega t - k_{zn} z)} \tag{2-9}$$

Where k_{zn} has the form of equation (2-10).

$$k_{zn} = k_{z0} + \frac{2\pi}{P} n \tag{2-10}$$

So the fields (electric and magnetic) in the periodic structure can be seen as a summation of an infinite number of fields with the same frequency but different wavelengths which are called spatial harmonics. Equation (2-9) and equation (2-10) are called the Floquet's equations. $\lambda_n = \frac{2\pi}{k_{zn}}$, and $E_n(x, y)$s electric fields are called spatial harmonics. The phase velocity and group velocity of each spatial harmonic in the periodic structure can be calculated as equation (2-11) and (2-12).

$$v_{p_n} = \frac{\omega}{k_{z0} + \frac{2\pi}{P} n} \tag{2-11}$$

$$v_g = \frac{\partial \omega}{\partial k_{zn}} = \frac{\partial \omega}{\partial k_{z0}} \tag{2-12}$$

From equation (2-12) the group velocities of all spatial harmonics are the same.

To explain the backward wave propagation, here an example of a waveguide that supports backward wave propagation is illustrated [34]. The waveguide is loaded with vanes which are separated axially with a period P shown in Figure 2-5. Adding corrugations/vans, changes the impedance of the structure and changes the phase velocity of the waveguide. Adding the metal vanes in the waveguide width direction, behaves like a capacitive load. As the wave propagates inside the waveguide, it experiences multiple reflections from the vanes with a phase change of 180 degree for the reflected electric field from each vane. When the reflection from the vanes add constructively in phase, they produce a stopped band in frequency. So, loaded waveguides behave like filters.

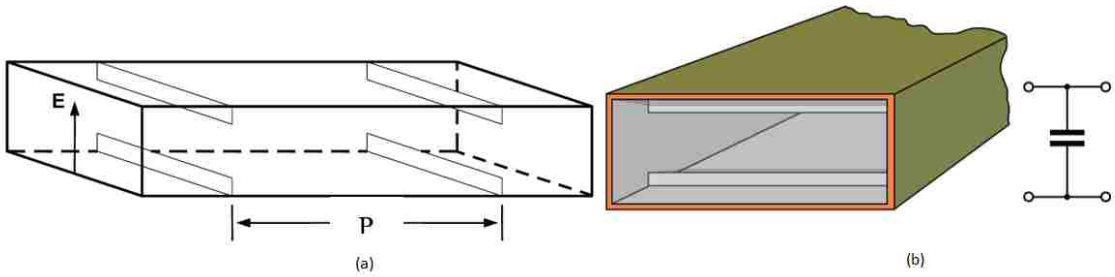

Figure 2-5 (a)Rectangular Waveguide loaded with vanes in its width direction and (b) its equivalent circuit

When the frequency is close to ω_c(cut-off of not loaded waveguide), the phase velocity is high (close to ∞) and the wavelength is much longer than P ($\lambda_g \gg P$), hence the reflections from the vanes do not add in phase. That is why so close to ω_c, the dispersion diagram is like a rectangular waveguide (without any loads).

As frequency increases, at some point λ_g becomes equal to 2P ($k_z P = \pi$), so the phase shift of a round trip of a reflected wave, between vanes, approaches 180 degrees and since there is another 180 degree reflected electric field from each vane, these reflections add in phase when $\lambda_g = 2P$, to create a stopband and hence there is no propagation and the group velocity goes to zero.

When $k_z P < \pi(\lambda_g > 2P)$ (before the stop band), the phase velocity is higher than when $k_z P = \pi(\lambda_g = 2P)$, and the wavelength is longer, hence, according to Figure 2-6, the maximum peak of forward wave is leading the maximum peak of backward wave and therefore the summation of the reflected and incident wave results in a forward wave.

When $k_z P > \pi(\lambda_g < 2P)$, the backward wave is moving with the same frequency as the forward wave, but since the wavelength is smaller than 2P, the backward wave is leading and the total field is a backward wave.

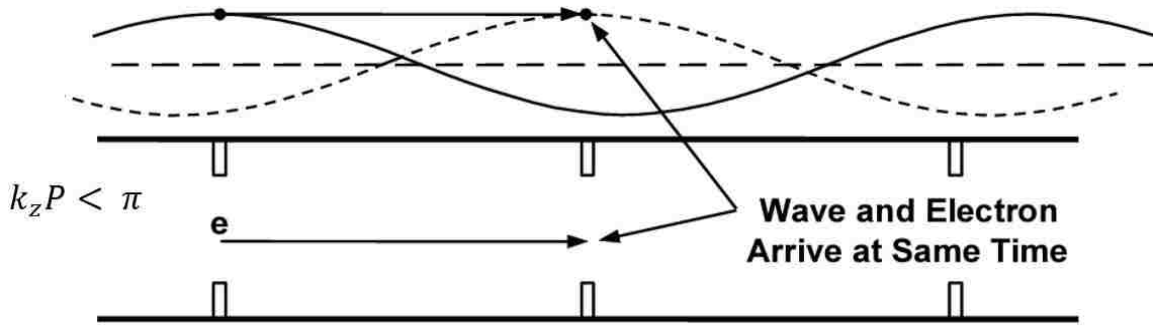

Figure 2-6 Backward wave dispersion in a periodically loaded waveguide [40]

Using the above explanation, the dispersion diagram of the vanes-loaded waveguide is deviates from that of an empty waveguide as shown in Figure 2-7.

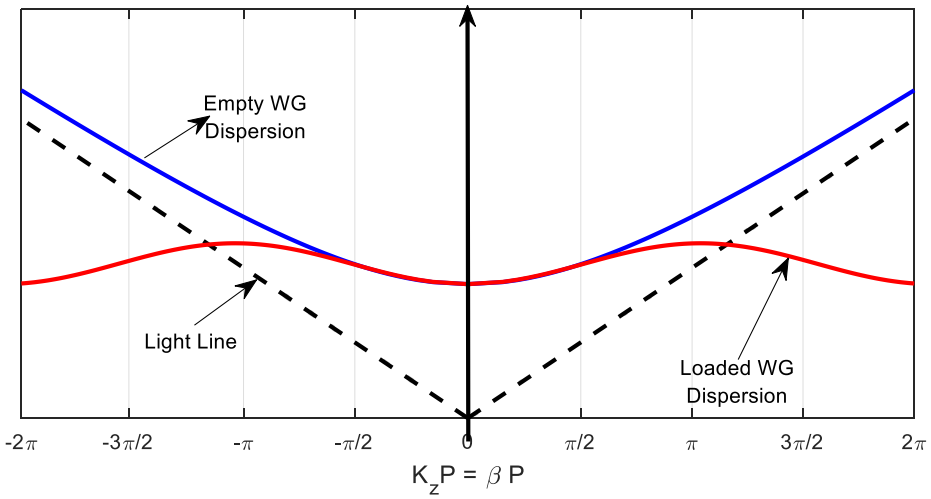

Figure 2-7 Dispersion Diagram of Iris Loaded Waveguide

2.5 Electron Beam in metamaterial Loaded Cylindrical Waveguide

As it was mentioned earlier, it is desired to use a metamaterial as slow wave structures in a BWO design. In this section, the general electromagnetic solution of a metamaterial filled Cylindrical waveguide when the electron beam passes through it is presented. Assume a circular waveguide of radius r is filled with an artificial dielectric which has a permittivity and permeability given by equations (2-13) and (2-14).

$$\bar{\bar{\varepsilon}} = \varepsilon_0 \begin{bmatrix} \varepsilon_{rr} & 0 & 0 \\ 0 & \varepsilon_{\varphi\varphi} & 0 \\ 0 & 0 & \varepsilon_{zz} \end{bmatrix} \tag{2-13}$$

$$\bar{\bar{\mu}} = \mu_0 \begin{bmatrix} \mu_{rr} & 0 & 0 \\ 0 & \mu_{\varphi\varphi} & 0 \\ 0 & 0 & \mu_{zz} \end{bmatrix} \tag{2-14}$$

Also assume an electron beam of radius r_b passing through the axis of circular waveguide. Momentum and continuity equations for the waveguide can be written as equations (2-15) and (2-16).

$$-\frac{\overrightarrow{\partial p}}{\partial t} = -e\vec{E} - e\vec{v} \times (\overrightarrow{B} + \overrightarrow{B_0}) \tag{2-15}$$

$$\frac{\partial n}{\partial t} + \nabla.(n\vec{v}) = 0 \tag{2-16}$$

where $\vec{p} = \gamma m_0 \vec{v}$, is the electron beam momentum, m_0 is the electron mass, γ is the relativistic factor, n is electron density, e is the electron charge, $\vec{v}$ is the electron velocity, $\vec{E}$ the electric field, $\vec{B}$ is the time harmonic magnetic field, and $\overrightarrow{B_0}$ is the static magnetic field that confines the electron beam.

Using perturbation theory, the unknown electron density and electron velocity can be written as a summation of equilibrium values and perturbed values as equations (2-17) and (2-18).

$$n = n_0 + n_1 \tag{2-17}$$

$$\vec{v} = \vec{v}_0 + \vec{v}_1 \tag{2-18}$$

Equilibrium (initial) values do not contribute to wave generation. The relativistic factor γ can be expanded as equation (2-19).

$$\gamma = \frac{1}{\sqrt{1 - \frac{v^2}{c^2}}} \approx \gamma_0 + \gamma_0^3 \beta_0^2 \frac{v_1}{v_0} \tag{2-19}$$

where $\gamma_0 = \frac{1}{\sqrt{1-\beta_0^2}}$, $\beta_0 = \frac{v_0}{c}$, c is the speed of light, and v_0 is electron beam velocity. Since the static magnetic field guides the electron beam in the axial direction, it is assumed that $\vec{v} = v_z \overrightarrow{a_z}$, and because we are solving the problem for a TM mode ($E_z \neq 0$), if we assume that the waveguide is uniform in the z direction and that the fields propagate in the z direction as $e^{-ik_z z}$, equations (2-15) and (2-16) can be simplified as equations (2-20) and equation (2-21):

$$im_0 v_1 \gamma_0^3 (\omega - k_z v_0) = eE_z \tag{2-20}$$

$$n_1(\omega - k_z v_0) - k_z v_0 v_1 = 0 \tag{2-21}$$

Solving equation (2-20) and equation (2-21) for the electron beam density results in equation (2-22).

$$\vec{J} = -en\vec{v} = \frac{-\omega e^2 n_0 E_z}{im_0 \gamma_0^3 (\omega - k_z v_0)^2} \overrightarrow{a_z} \tag{2-22}$$

On the other hand, Maxwell's equation for a time harmonic current and charge free medium, are simplified as (2-23).

$$\nabla \times \vec{E} = -i\omega\bar{\bar{\mu}}\vec{H} \tag{2-23}$$

$$\nabla \times \vec{E} = -i\omega\bar{\bar{\mu}}\vec{H}$$

In this dissertation we are interested in the TM_{0n} modes solution, with E_z, E_r and H_φ being the only nonzero existing components and $\frac{\partial E}{\partial \varphi} = \frac{\partial H}{\partial \varphi} = 0$. Maxwell's equations are simplified as equation (2-24) and (2-25).

$$(-ik_z E_r - \frac{\partial E_z}{\partial r})\vec{a}_\varphi = -i\omega\bar{\bar{\mu}}(H_\varphi \vec{a}_\varphi) \tag{2-24}$$

$$ik_z H_\varphi \vec{a}_r + \vec{a}_z\left(\frac{1}{r}\frac{\partial(rH_\varphi)}{\partial r}\right) = i\omega\bar{\bar{\varepsilon}}(E_r\vec{a}_r + E_z\vec{a}_z) \tag{2-25}$$

Solving the above Maxwell equations (2-26), (2-27), (2-28) gives the value of E_r, E_z and H_φ respectively.

$$E_r = \frac{k_r k_z}{\omega\mu_{\varphi\varphi}\varepsilon_{rr}} J_0'(k_r r)e^{-ik_z z} \tag{2-26}$$

$$E_z = i\frac{k_r^2}{\omega\mu_{\varphi\varphi}\varepsilon_{zz}} J_r(k_r r)e^{-ik_z z} \tag{2-27}$$

$$H_\varphi = \frac{k_r}{\mu_{\varphi\varphi}} J_0'(k_r r)e^{-ik_z z} \tag{2-28}$$

Substituting the E_z from equation (2-27), the electron current beam density from equation (2-22), can be derived as equation (2-29).

$$\vec{J} = -en\vec{v} = \frac{-\omega e^2 n_0}{m_0\gamma_0^3(\omega - k_z v_0)^2}\frac{k_r^2}{\omega\mu_{\varphi\varphi}\varepsilon_{zz}} J_r(k_r r)e^{-ik_z z}\overrightarrow{a_z} \tag{2-29}$$

2.6 Electron Generation

To generate electron beams passing through a slow wave structure, electrons must be detached from atoms. Then, the separated electrons are guided with the confining static magnetic field through the structure of interest. To separate the electrons from their atom orbits several types of mechanisms has been introduced such as field-emission, thermionic emission, photo-emission, secondary emission or explosive emission.

When the electron beam is generated, the electron beam current is also limited to a maximum value. It can be shown that for a narrow pencil beam, which the electron beam potential is not varying along beam radius, the Child-Langmuir axial space-charge-limiting is calculated through equation (2-30)

$$I_{max} = \frac{mc^2}{e\eta_0} \frac{2\pi}{\ln\left(\frac{R}{R_b}\right)} (\gamma_0^{\frac{2}{3}} - 1)^{\frac{3}{2}} \tag{2-30}$$

Increasing currents beyond I_{max} limit, will lead to virtual cathode formation.

2.6.1 Explosive Emission

Explosive emission provides the most accurate model to what happens in the experiment. This emission occurs when plasma is formed around the cathode and the electric field strength exceeds the threshold value of typically $100kv/m$ which starts electron emission. The cathode surface has microscopic protrusions that in the presence of high voltage generate electric field enhancement at those protrusions. The electric filed when exceeds $100kv/m$ causes high-field emission.

3 Chapter 2 Group theory

In this chapter, we outline the general description and symmetry concepts defined in group theory. First the general features of group theory are explained. Next, how symmetry properties of metamaterials can be used to identify their electromagnetic properties are explained. Several well-known metamaterial structures are analyzed using group theory. Moreover, how group theory can be utilized in synthesizing metamaterials with desired constitutive properties is demonstrated. Finally, the basic steps for designing, phase shifters, polarization rotators, and HPM sources using metamaterials and group theory are presented and discussed.

3.1 Group Theory Background

Group theory has been used in chemistry to classify molecules based on their symmetry properties. Group theory explains how the symmetry properties of a molecule such as molecular orbital properties, its active vibrational modes, the active bands of infrared (IR), Raman spectrum, etc., are related to its symmetry properties.

Molecule behavior in chemistry can be seen as equivalent to metamaterial unit cells in electromagnetics. Using this analogy, molecular modes of vibration are corresponding to the resonant modes of metamaterial. Therefore, group theory can be used to determine the electromagnetic properties of metamaterials. However, there are some limitations in using group theory for designing unit cells for periodic structures [41]. First, the group theory derivation is based upon the assumption of slowly varying external electromagnetic waves on a periodic structure, thus, incident fields need to be quasistatic

along the unit cell. So, if a is the unit cell largest dimension and λ is the incident EM field wavelength, the condition $a/\lambda < 0.2$ need to be satisfied, to use group theory for analyzing and designing metamaterial structures. Second, group theory can predict the general elecrtomagnetic behavior of a metamaterial, but the exact value of permeability and permittivity and the exact resonance frequencies of the specific metamaterial structure need to be extracted through full wave EM simulation trough retrieval of electromagnetic properties using scattering parameters [25].

In this work, group theory is also shown how to be applied specifically to complimentary metallic metamaterial structures for high power microwave applications. This work has not been reported before in literature.

3.1.1 Symmetry Elements

For any object like a molecule or a metamaterial unit cell, various kinds of symmetry operations can be performed. An object is defined as symmetric if various symmetry operations, such as axial rotation, mirror plane reflection, center point inversion, etc., preserve the object geometry undergoing the symmetry operation. The main symmetry operations can be categorized in five groups:

Identity (**E**). All structures possess the identity symmetry operation. By applying the Identity symmetry operation, no change occurs to the metamaterial geometry (every part of the metamaterial structure stays in the same place).

Proper n-Fold Rotations($\boldsymbol{C_n}$). This operation is rotation by 360°/n (n is an integer) about an axis, where n is any integer number. For example, C_2 means a 180° rotation, C_3 means 120° rotation about any x, y or z axis. The axis with largest n in an object is its principal axis. Figure 3-1 shows a $\boldsymbol{C_2}$ rotation (180 degree).

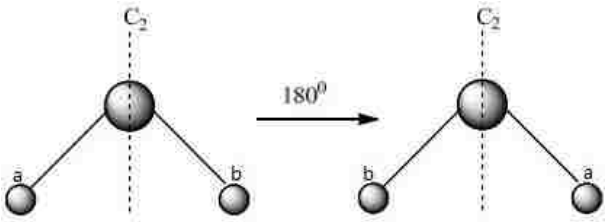

Figure 3-1: 2-fold rotation C_2.

Reflection/Mirror plane (**σ**), when a reflection through a mirror plane, preserves object geometry, it said to have mirror plane symmetry. If the mirror plane contains the principal rotation axis, it is called a vertical mirror plane $\boldsymbol{\sigma_v}$, whereas the mirror plane which is perpendicular to the principle axis, is called horizontal mirror plane $\boldsymbol{\sigma_h}$. Figure 3-2 shows how mirror plane brings a molecule to the same geometry.

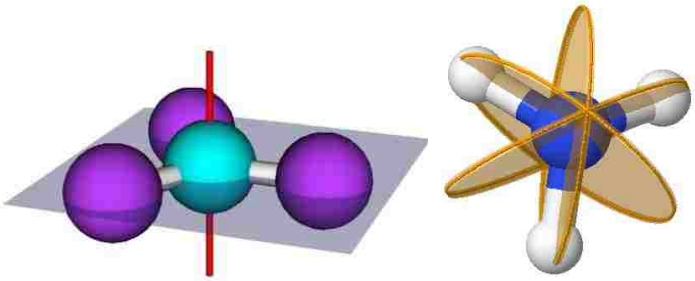

Figure 3-2: Reflection mirror plane.

Inversion (**i**). An object has an inverse center if its geometry is unchanged when reflected through a single point. The point is the symmetry element for inversion. Inversion point is the symmetry element. Figure 3-3 shows inversion symmetry element applied on a molecule.

Figure 3-3: Inversion center and symmetry of a molecule.

Improper n-Fold Rotation ($\mathbf{S_n}$). A combination of two successive operations, first proper rotation C_n and then reflection $\boldsymbol{\sigma_h}$ is called improper rotation. Figure 3-4 shows how with a C_4 rotation (90-degree rotation) followed by mirror reflection plane, the molecule is still unchanged.

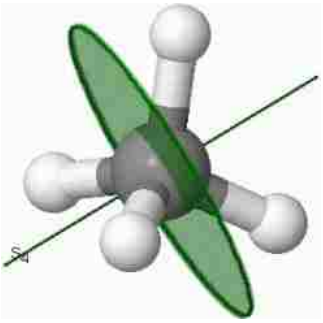

Figure 3-4: a S_4 rotation (C_4 $plus$ $\boldsymbol{\sigma_h}$ mirror plane).

3.1.2 Symmetry point group

Any structure/molecule/metamaterial can be classified according to the set of symmetry elements they have. The collection of symmetry elements for a molecule form its "point group". Figure 3-5 is the flow chart to define the point group of any structure. [42], [43].

3.1.3 Character Table

A character table summarizes all information for a point group, including its symmetry operations and irreducible representations. It is a square matrix of all symmetries in the corresponding point group. The character table is square because always numbers of irreducible representations is equal to the number of classes of symmetry operations. The table shows how a particular irreducible representation transforms when a particular symmetry operation is applied.

Table 3-1 shows an example of a character table. The first column of the table (A, B_1, B_2, B_3) are irreducible representation labels. In front of each is a vector, for example $B_1 = (1, 1, -1, -1)$, which is irreducible representation vector. These are basis vectors which are orthogonal, linearly independent and form the basis modes of the structure; which any other mode (reducible representation) of the metamaterial/molecule can be written as a linear combination of these basis representation. More details about how to calculate the character table can be found in chemistry references [44].

Table 3-1 Character table for D_2 point group.

	E	C_2 (z)	C_2 (y)	C_2 (x)	linear, rotations	quadratic
A	1	1	1	1		x^2, y^2, z^2
B_1	1	1	-1	-1	z, R_z	xy
B_2	1	-1	1	-1	y, R_y	xz
B_3	1	-1	-1	1	x, R_x	yz

3.2 Metamaterial Analysis Using Group Theory

In this section using group theory, a step by step procedure, is presented that is used to predict the electromagnetic behavior of a metamaterial structure. The case where a specific structure is analyzed with group theory is referred to here as the "forward-problem" approach. Later on it will be shown how group theory can be used to synthesize the metamaterial structure based on desired spectral EM properties, including specific permittivity and permeability tensors.

First, given a specific metamaterial geometry, we can find its symmetry operations and determine the metamaterial symmetry "point group". A methodology has been developed to find the symmetry point group of any structure. The specific steps to

achieve this are shown in Figure 3-5. Second, using the "character table" one can determine which modes and electromagnetic behaviors are possible in the given metamaterial. The character table simply gives the available potential modes but that does not guarantee that all of them are also active modes as well. Finally, a set of "basis currents" are determined on the metamaterial structure. Once the currents are defined, symmetry operations are applied again on these basis currents to define the primary ones, referred to here as the "irreducible" ones. Any possible existing current on the structure can be written as the linear combination of the irreducible currents. Based on these linear combinations one can determine the possible active modes out of a set of potential modes [42], [43].

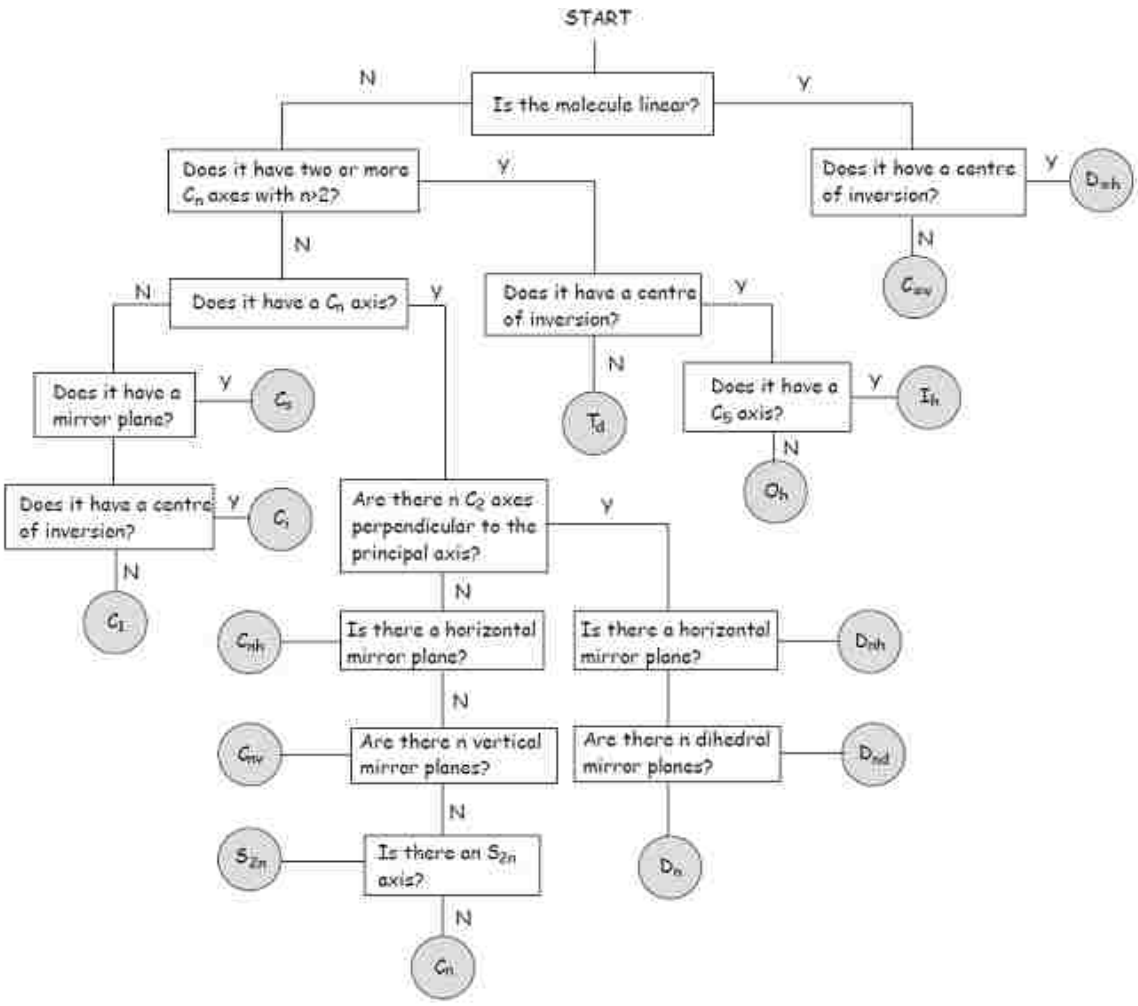

Figure 3-5: Decision chart to find symmetry group of a metamaterial.

3.2.1 SRR Behavior Analysis Using Group Theory

An SRR geometry is shown in Figure 3-6. This SRR has the $\{E, C_2(z), C_2(x), \sigma_{xy}, \sigma_{xz}\}$ set of symmetry operations. Figure 3-7 shows that an SRR has 4 symmetry operations described by $\{E, C_2(z), C_2(x), \sigma_{xy}, \sigma_{xz}\}$. From Figure 3-5, one can see that it belongs to C_{2v} point groups.

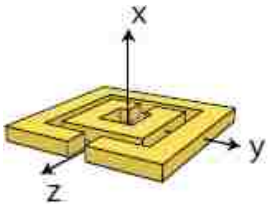

Figure 3-6: Split ring resonator geometry.

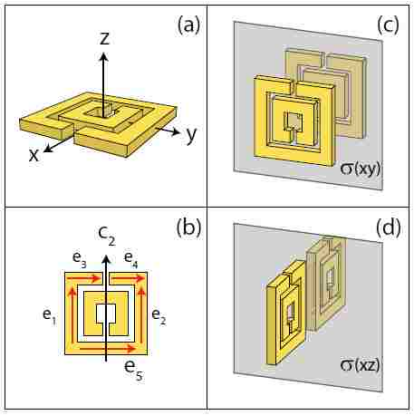

Figure 3-7: Spit ring resonator and its symmetry operations.

The character table of C_{2v} point group is shown in Table 3-2.

Table 3-2: Character table for C_{2v} point group.

	E	C_2 (z)	σ_v(xz)	σ_v(yz)	linear, rotations	quadratic
A_1	1	1	1	1	z	x^2, y^2, z^2
A_2	1	1	-1	-1	R_z	xy
B_1	1	-1	1	-1	x, R_y	xz
B_2	1	-1	-1	1	y, R_x	yz

3.2.2 Principles of Group Theory

The relationship between the electric/magnetic flux density and electric/ magnetic fields in materials is expressed through the following tensor (3-1).

$$\begin{bmatrix}\bar{D}\\ \bar{B}\end{bmatrix} = \begin{bmatrix}\bar{\bar{\varepsilon}} & \bar{\bar{\xi}}\\ \bar{\bar{\zeta}} & \bar{\bar{\mu}}\end{bmatrix}\begin{bmatrix}\bar{E}\\ \bar{H}\end{bmatrix}, \text{ where } \bar{\bar{\varepsilon}} = \begin{bmatrix}\varepsilon_{xx} & \varepsilon_{xy} & \varepsilon_{xz}\\ \varepsilon_{yx} & \varepsilon_{yy} & \varepsilon_{yz}\\ \varepsilon_{zx} & \varepsilon_{zy} & \varepsilon_{zz}\end{bmatrix} \quad 3\text{-}1)$$

$\bar{\bar{\varepsilon}}$ and $\bar{\bar{\mu}}$, are the permittivity and permeability tensor while, $\bar{\bar{\xi}}$ and $\bar{\bar{\zeta}}$ define the magnetoelectric tensor representing the cross relation between electric and magnetic flux. The first column lists the symbols of irreducible representations of C_{2v} point group. The character irreducible representations for each symbol is the vector in front of it (1s and -1s). From the electromagnetics point of view, each row represents a metamaterial mode. Each two mode vectors are orthogonal, linearly independent and form the basis modes of the structure. The first row define the symmetry operations of the metamaterial. The last column contains linear and quadratic terms equivalent to that irreducible representation in row. The last two columns are named basis vectors. These vectors can excite the mode symbol in that row. The way basis vector is transformed by the symmetry operations of the character table, is used to determine basis vectors for each mode. For example, from Table 3-2 one can predict in order to excite mode A_1, electric field E_z is needed as excitation, while B_1 can be excited with either $E_x \; and \; H_y$. According to Maxwell's equations, the electric field is linear (parallel) with the current, so in the character table when there is r = $\{x, y \; or \; z\}$ in the last two columns, it means that the irreducible representation (mode) can be excited by $E_r = \{E_x, E_y \; or \; E_z\}$. Similarly, the magnetic field is axial with the current, and in a current loop, the magnetic field is perpendicular to the current plane. So, the magnetic field is transformed under the rotation $R_r =$

$\{R_x, R_y \ or \ R_z\}$. So to excite the mode with R_r, in the row, a magnetic field in the r direction is required [45]. The electromagnetic constitutive tensor has four quadrants shown in Figure 3-8. The tensor elements correspond to metamaterial EM constitutive elements in the following way:

- The diagonal ε elements are expressed by the independent variable r (r can be x, y, or z which express linear modes) For example, if there is a separate y in one of the modes in the character table of a metamaterial, then the mode is active and the metamaterial is expected to show $\varepsilon_{yy} < 0$ with a E_y excitation field.
- The diagonal μ terms are independent of R_r in the character table (r is x, y, or z). So, an independent R_z in the metamaterial character table, if the mode is active, predicts that $\mu_{zz} < 0$ with a H_z excitation.
- (r_i, r_j) and (R_{r_i}, R_{r_j}), where $i \neq j$ show off-diagonal ε and μ elements respectively, which are simultaneous and coupled modes. For example, from (x, y) in the character table of a structure, it can be inferred, with E_x excitation, that $\varepsilon_{xx} < 0, \varepsilon_{xy} < 0, \varepsilon_{yx} < 0$ is predicted, to have $\mu_{yy} < 0$, excitation E_y is needed.
- r_i, r_j or R_{r_i}, R_{r_j} terms (without parentheses) are simultaneous but not coupled modes (independent modes). x, y shows only $\varepsilon_{xx} < 0$ or $\mu_{yy} < 0$ depending on excitation field direction.
- r_i, R_j indicates ζ and ξ elements. y, R_x term in an active mode, with E_y excitation shows $\varepsilon_{yy} < 0 \ and \ \zeta_{xy} < 0$.

It needs to be emphasized again that group theory predicts the overall electromagnetic behavior of a metamaterial not the exact value of resonance frequency, permeability or permittivity. The values of thse parameters for any specific metamaterial are functions of its size. The exact parameters values can be extracted through full wave EM simulation and with retrieval of electromagnetic properties using scattering parameters. Also, the exact values of tensors cannot be determined by group theory and they can only be calculated through simulation and they depend on the

material dimensions as well as geometry. Finally, if reciprocity holds in one structure, $\xi^T = -\zeta$ should be satisfied.

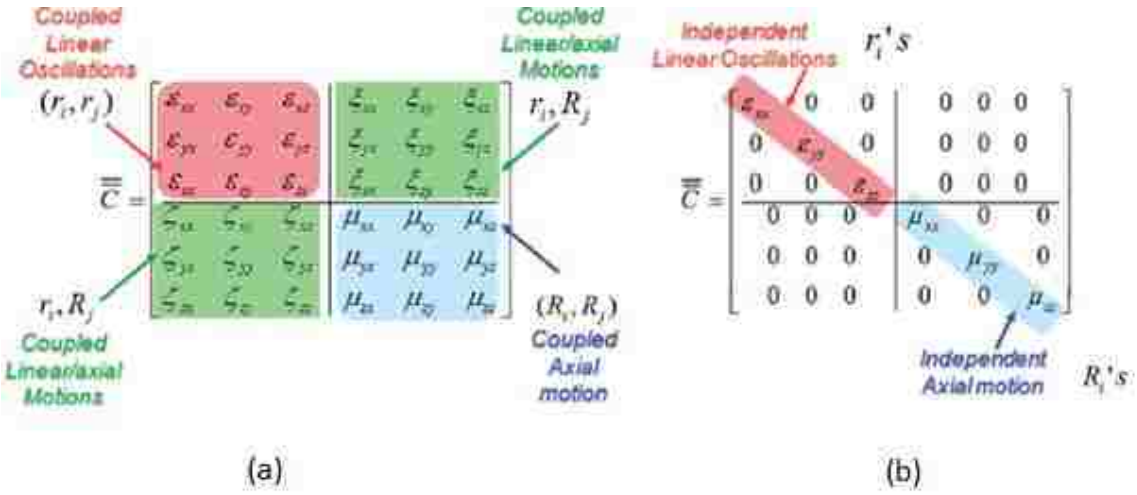

Figure 3-8: a) Four quadrants of the electromagnetic constitutive tensor and b) their corresponding linear and axial terms in the character tables from [45]

3.2.3 Basis Current in Split Ring Resonators

As its was shown earlier the character table only gives the potential modes of a metamaterial. To find the resonant active mode of a structure, first, a set of basis current that can flow on the unit cell must be defined. The current sets are all the possible current vectors that can be on the structure. Figure 3-9 shows the basis current vectors of a SRR. Selecting the direction of these current vectors is arbitrary.

The symmetry operations of C_{2v} in character table are applied on the chosen current sets. In Figure 3-9, one can see how the current sets are affected by each symmetry operation. For each symmetry operation, three possible cases can occur:

1. If the basis current vector, has the same direction and same location after the symmetry operation is applied, a "+1" is assigned to that current segment.

2. If the current vector is mapped to its opposite direction and preserves its location, a "−1" is assigned to that current.
3. If the current does not remain in the same location after a symmetry operation is applied, a "0" is assigned to it.

For each symmetry operation, the 1, -1 and zeros are added up to form a character number for that symmetry operation. For example, since the identity operation (E) keeps each current in the same location and direction, the character for each current is +1, thus the character number for identity operation is always equal to number of current vectors.

For a proper axial rotation in $C_2(x)$, the basis currents e_9 and e_{10} are mapped to their opposite sign so the character for $C_2(x) = -2$, etc. Using the procedure mentioned above, the characters of the basis will be like the ones shown in Figure 3-9.

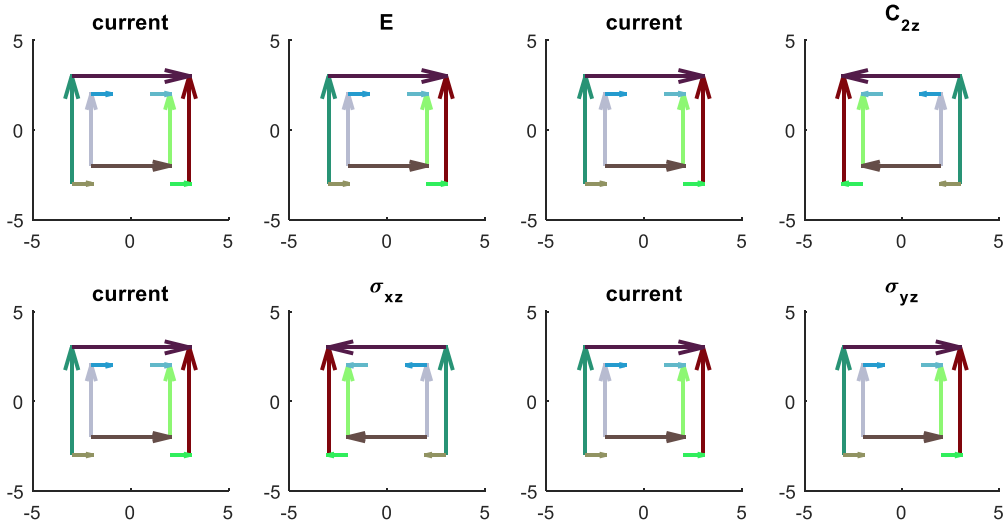

Figure 3-9: Behavior of SRR basis currents under symmetry elements of C_{2v} group.

The character of the chosen basis currents on SRR is shown in Table 3-5.

Table 3-3: Characters of the basis currents for SRR.

symmetry	E	$C_2(z)$	$\sigma_v(xz)$	$\sigma_h(yz)$
Character (χ)	10	-2	-2	10

As mentioned before, the irreducible representations are basis vectors that any vector, including the character of basis currents $\vec{\chi} = (10, -2, -2, 10)$, can be written as a linear combination of the basic irreducible representations. Applying the concept of the Orthogonality Theorem [46] to determine the coefficient of each Irreducible representation in linear combination a_m

$$a_m = \frac{1}{h}\sum_i n_i \, \chi(i)\chi_m(i) \qquad 3\text{-}2)$$

Where h is the number of symmetry operations in the point group, n_i is the number of symmetry operations in each class i, χ is the character of a reducible representation, and χ_m is the character of the irreducible representation.

$\vec{\chi} = (10, -2, -2, 10) = 2 \times [2 \times (1, 1, 1, 1) + 3 \times (1, -1, -1, 1)]$ so, the normalized active modes can be shown as (3-3).

$$\Gamma = 2A_1 + 3B_2 \qquad 3\text{-}3)$$

The modes of the SRR design are generated by applying the symmetry operations, as shown in

$$\begin{bmatrix} \varphi'(A_1) \\ \varphi'(A_2) \\ \varphi'(B_1) \\ \varphi'(B_2) \end{bmatrix} = \begin{bmatrix} 1 & 1 & 1 & 1 \\ 1 & 1 & -1 & -1 \\ 1 & -1 & 1 & -1 \\ 1 & -1 & -1 & 1 \end{bmatrix} \begin{bmatrix} e_1 & e_2 & e_3 & e_4 & e_5 & e_6 & e_7 & e_8 & e_9 & e_{10} \\ e_2 & e_1 & -e_4 & -e_3 & -e_5 & e_7 & e_6 & -e_9 & -e_8 & -e_{10} \\ e_2 & e_1 & -e_4 & -e_3 & -e_5 & e_7 & e_6 & -e_9 & -e_8 & -e_{10} \\ e_1 & e_2 & e_3 & e_4 & e_5 & e_6 & e_7 & e_8 & e_9 & e_{10} \end{bmatrix}$$

The fact that two different active representation modes exist means that these two modes are simultaneously active but occur at different frequencies.

Considering the character table for the C_{2v} point group we see that an electric field vector polarized along the z direction, transforms as A_1, and y-polarized light transforms as B_2 symmetry. The function R_α represents a rotation about the α axis, where α =x, y, z. Thus, a magnetic field (axial) vector, polarized along the x-direction, also transforms as B_2

symmetry. In Figure 3-10 a summary of the SRR direction and retrieval permeability and permittivity is presented.

Case 1) (E_x, H_y), By studying the C_{2v} character table, these two fields do not excite any modes because in group theory, they can only excite the B_1 mode. As it can be seen from $\Gamma = 2A_1 + 3B_2$ because of basis currents distribution and symmetry operation B_1 mode has been cancelled out.

Case 2) (E_x, H_z), Having C_{2v} character table, these two fields do not excite any mode because they only can excite A_2 or B_1 modes. As it can be seen from $\Gamma = 2A_1 + 3B_2$

Case 3) (E_y, H_x), considering C_{2v} character table, these two fields have excited the structure. These two fields can excite $B_2(y, R_x)$ mode. As it can be seen from $\Gamma = 2A_1 + 3B_2$, B_2 mode is active. From Figure 3-8, we predict that structure will have $\varepsilon_{yy}, \mu_{xx}, \xi_{yx}\ and\ \zeta_{xy}$. It is evident that SRR with (E_y, H_x) excitation combination, exhibit a magnetoelectric effect.

Case 4) (E_y, H_z), Considering C_{2v} character table, E_y Field can excite $B_2(y, R_x)$ mode while the H_z can excite $A_2(z)$ in the structure. But as it can be seen from $\Gamma = 2A_1 + 3B_2$, because of basis currents distribution and symmetry operation only B_2 mode is active. Therefore, it will be predicted that only ε_{yy} and ζ_{xy} are active. It can be verified in Figure 3-10.

Case 5) $(E_z, H_x), E_z$ Field can excite $A_1(z)$ mode while the H_x can excite $B_2(y, R_x)$ in the structure. As it can be seen from $\Gamma = 2A_1 + 3B_2$, both $A_1\ and\ B_2$ modes are active. Therefore, it will be predicted that ε_{zz}, μ_{xx} and ξ_{yx} are active. Because they are different mode, the resonance behavior and therefore negative range of frequency do not coincidence. It can be verified from Figure 3-10 that only ε_{zz} is negative in some range of

frequency (about 24 GHz). Since the size of metamaterial is d = 2.5 mm here so the maximum frequency that both group theory and retrieval codes are valid is when $d \leq \frac{\lambda}{5}$ and it means $f_{max} \leq \frac{c}{5d} \Longrightarrow f_{max} \leq 24\,GHz$ which means that even ε_{zz} in negative, it is preferred to avoid frequencies above that since quasi-static behavior is not valid any more.

Case 6) $(E_z, H_y), E_z$ Field can excite the $A_1(z)$ mode while the H_y can excite $B_1(x, R_y)$ in the structure. As it can be seen from $\Gamma = 2A_1 + 3B_2$, only the A_1 mode is active. Therefore, it is predicted that only ε_{zz} can be seen in EM constitutive parameter retrieval. As it was seen from the previous case, we expect a resonance behavior of ε_{zz} to happen at a higher frequency (Figure 3-10).

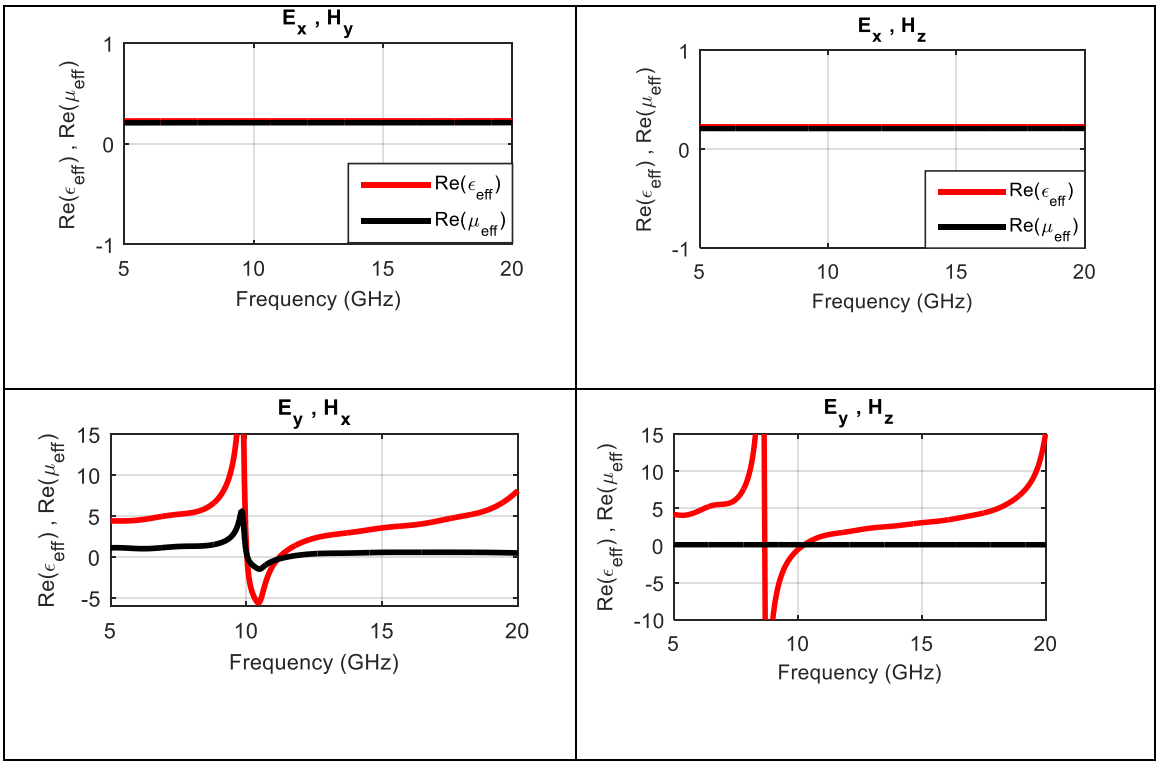

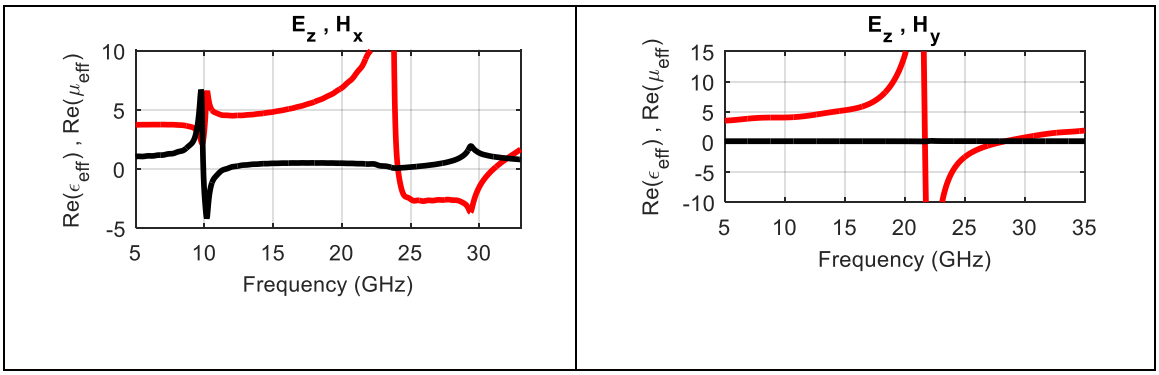

Figure 3-10: Split Ring Resonators permittivity and permeability for different excitation.

3.3 Inverse Problem Solving Using Group Theory

Group Theory is powerful when it comes to dealing with the inverse-problem approach, where the geometry of the metamaterial unit cell can be engineered to produce a desired electromagnetic constitutive tensor. The Flowchart in Figure 3-11 shows the inverse problem procedure for designing a metamaterial topology based on desired $\bar{\bar{\varepsilon}}$, $\bar{\bar{\mu}}$, $\bar{\bar{\xi}}$ *and* $\bar{\bar{\zeta}}$ tensors.

First, in the tensor matrix, those elements that are desired to have a value (nonzero elements) is chosen. Active tensor elements will reveal the form of the desired EM interaction. The necessary EM interaction, determines the linear and axial terms in the metamaterial character table. From the required linear and axial terms, we chose the simplest symmetry group which include the required linear and axial terms. We can design a metamaterial with any specified symmetry operation. The procedure used in this dissertation, is a genetic algorithm-based approach that can be used to design a structure with a desired symmetry operation. The actual approach will be explained in detail, in the next section. Finally, to verify that the metamaterial modes of interest are active, the irreducible representation of the metamaterial is calculated following the procedure

explained earlier In the case that the desired modes are not active, the metamaterial needs to be modified to activated desired modes.

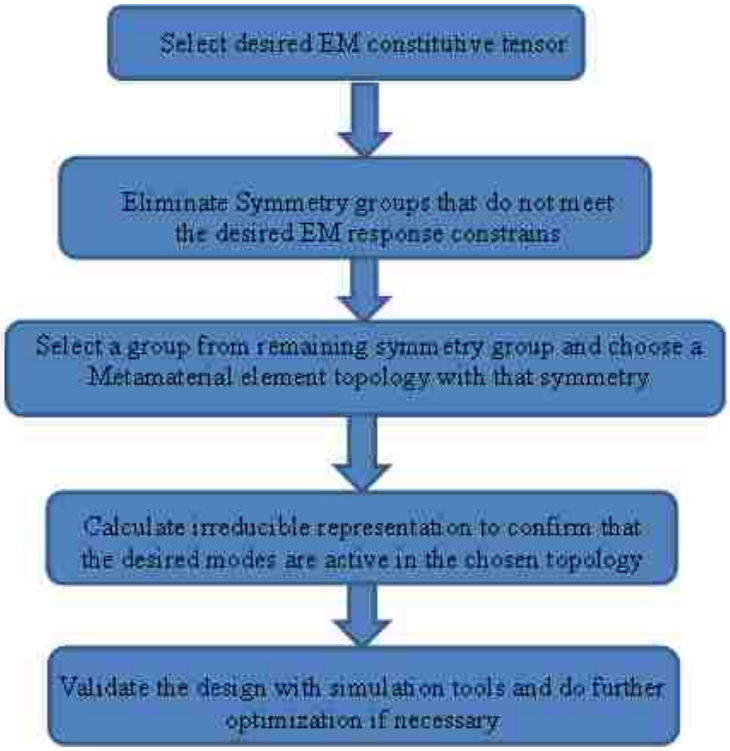

Figure 3-11: Flowchart outlining the inverse-problem steps for using group theory to design a metamaterial with a desired electromagnetic constitutive EM parameter.

3.4 Design an ideal Metamaterial

As the last topic, we focus on designing an ideal metamaterial is a metamaterial with no magneto optical behavior which has both negative permittivity and negative permeability in the same range of frequency.

In [47] a metamaterial design is published which claims to have simultaneous negative permeability and permittivity in the same range of frequency and so it is a negative index metamaterial. Also in the same paper, the authors claim that the design is an isotropic 3D metamaterial (no magneto optical response). Here using group theory, we will explain why the proposed metamaterial is not capable to have negative index and the presented results have an error due to software inaccuracy. Instead, an alternative design will be

proposed that can create a material with both negative permeability and permeability at the exact same frequency.

From the group theory point of view this means the MTM unit cell should belong to a group which possesses linear and axial basis functions that occur in the different irreducible modes to assure they are not coupled and that $\bar{\bar{\xi}} = 0 \; and \; \bar{\bar{\zeta}} = 0$. Therefore, no magneto optical behavior exists. But the fact that the linear mode (electric mode) and the axial mode (magnetic mode) happen in different irreducible modes, means that they happen in different frequencies. So, this a challenge. Figure 3-12 shows the proposed metamaterial reported in [47]. The yellow part is metallic while the gray part is air. So, the proposed structure is a complementary metamaterial.

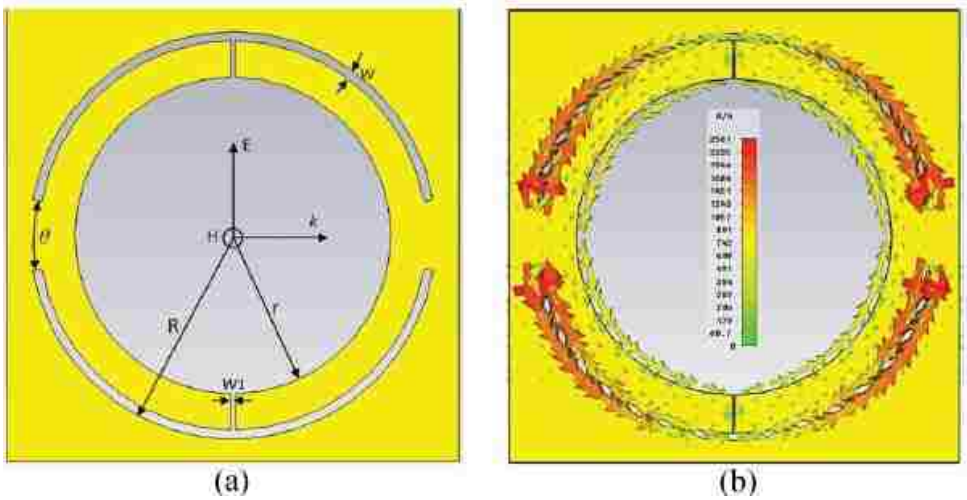

Figure 3-12: Complementary design in [47] in with dimensions R = 4.5 mm, r = 3.5 mm, w = 0.15 mm, $w1$ = 0.05 mm, θ = 20. (b) The current density of the complementary design at 9.9 GHz from [47].

3.5 Studying The Proposed Structure Using Group Theory

According to Figure 3-12 if the electric and magnetic field directions are (E_y, H_z, k_x), it can be seen that the symmetry operations for this structure

are $\{E, C_2(z), C_2(y), C_2(x), i, \sigma_{xy}, \sigma_{xz}, \sigma_{yz}\}$. Knowing the symmetry operations, we understand the proposed geometry belongs to D_{2h} point group. The character table for this point group is shown in Table 3-4.

Table 3-4: D_{2h} character table.

	E	C_2 (z)	C_2 (y)	C_2 (x)	i	σ (xy)	σ (xz)	σ (yz)	linear, rotations	quadratic
A_g	1	1	1	1	1	1	1	1		x^2, y^2, z^2
B_{1g}	1	1	-1	-1	1	1	-1	-1	R_z	xy
B_{2g}	1	-1	1	-1	1	-1	1	-1	R_y	xz
B_{3g}	1	-1	-1	1	1	-1	-1	1	R_x	yz
A_u	1	1	1	1	-1	-1	-1	-1		
B_{1u}	1	1	-1	-1	-1	-1	1	1	z	
B_{2u}	1	-1	1	-1	-1	1	-1	1	y	
B_{3u}	1	-1	-1	1	-1	1	1	-1	x	

Having the group theory principles explained in previous sections and the character table of D_{2h} point group, with (E_y, H_z, k_x) field excitation, the constitutive tensor can have the following matrix in equation (3-4), in the case that B_{2g} and B_{1u} modes are activated. However, since B_{2g} and B_{1u} are two different modes, we expect this metamaterial to have $\varepsilon_{yy} < 0$ in frequency f_1 and $\mu_{zz} < 0$ in frequency f_2 which $f_1 \neq f_2$. Also, considering the character table, the metamaterial in an isotropic with no magnetoelectric effect.

$$\begin{bmatrix} \bar{\bar{\varepsilon}} & \bar{\bar{\xi}} \\ \bar{\bar{\zeta}} & \bar{\bar{\mu}} \end{bmatrix} = \begin{bmatrix} 0 & 0 & 0 & 0 & 0 & 0 \\ 0 & \varepsilon_{yy} & 0 & 0 & 0 & 0 \\ 0 & 0 & 0 & 0 & 0 & 0 \\ 0 & 0 & 0 & 0 & 0 & 0 \\ 0 & 0 & 0 & 0 & 0 & 0 \\ 0 & 0 & 0 & 0 & 0 & \mu_{zz} \end{bmatrix} \quad 3\text{-}4)$$

To find the activate modes of the design, the basis current vectors of the structure is represented in the form of current segments on the square form of the structure, in Figure 3-13. Then each symmetry operation of the character table of the D_{2h} point group is applied

to the basis currents. The process is shown in Figure 3-13. Using the explained procedure in previous section, the characters of the basis will be like Table 3-5.

Table 3-5: characters of the basis currents for complementary metamaterial.

symmetry	E	$C_2(z)$	$C_2(y)$	$C_2(x)$	i	σ_{xy}	σ_{xz}	σ_{yz}
Character (χ)	28	0	-2	-2	0	28	-2	-2

applying the concept of the Orthogonality Theorem to determine how many times each Irreducible representation occurs; the active mode will be:

$$\Gamma = 6A_g + 8B_{1g} + 7B_{2u} + 7B_{3u} \qquad 3\text{-}5)$$

Therefore, from Γ and character table, since A_g, B_{1g}, B_{2u} and B_{3u} modes are active mode, also since the excitation fields are $E_y \; and \; H_z$, we have both see $\varepsilon_{yy} < 0 \; and \; \mu_{zz} < 0$. but they do not happen in the same frequency. The results presented in Figure 3-14 validates there in no negative index behavior.

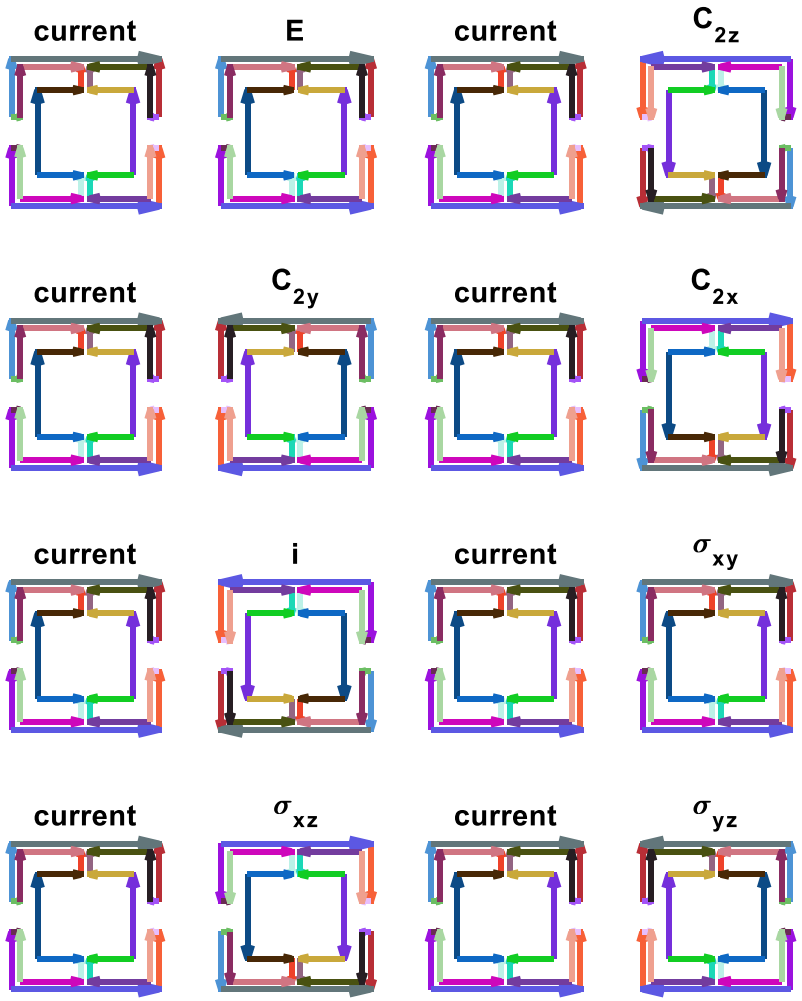

Figure 3-13: Behavior of metamaterial unit cell basis currents under symmetry elements of D_{2h} group.

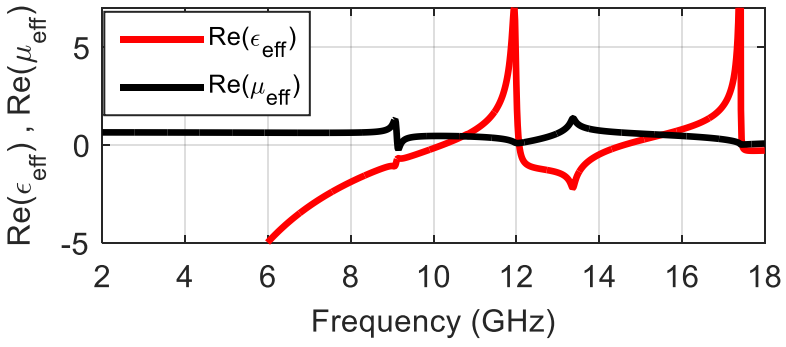

Figure 3-14: metamaterial negative permeability and permittivity in different frequencies.

3.6 Design

In SRR analysis part we showed that split ring resonators can have simultaneous negative permeability and permittivity with $E_y \; and \; H_x$ as the field excitation but it has bianisotropic (magnetoelectric response) behavior which is not desirable. In [48], Padilla, has proposed some unit cells just with negative permeability and no magneto-optical behavior, however he failed to design for a negative index of refraction. Also in [41], a systematic approach, based on group theory, was proposed to design isotropic magnetic metamaterials but again for materials with negative permeability only. To our knowledge in only report on designing isotropic negative index metamaterial is in [47] which proved to be just a simulation error. Here, for the first time an isotropic negative metamaterial is designed that later on will be used in designing an HPM source.

In the previous section, we showed that any isotropic material by itself cannot show DNG metamaterial in the same frequency, because, isotropic behavior requires the modes to be separate, and separate modes mean negative permeability and permittivity in different frequencies. Thus, designing a negative index metamaterial which is isotropic is still a challenge. The proposed metamaterial needs to also be easy to fabricate. The solution to this contradiction is a non-homogenous metamaterial. As it was explained earlier, for an isotropic metamaterial the negative permittivity and permeability occur in different frequency, therefore, if every other metamaterial unit cell dimension is scaled up/down then it can be engineered to show the negative permeability and permittivity in the same frequency. We call this metamaterial a dissimilar metamaterial.

Since, our main interest is a metamaterial for high power microwave environment, we are focusing on complementary metamaterials with no dielectric substrate. Dielectrics cannot survive HPM environment due to breakdown.

A proposed unit cell has been shown in Figure 3-15. The structure belongs to the D_{2h} group (Table 3-4) and the basis current under symmetry operation is as the one shown in Figure 3-13. Therefore, the active modes will be as

$$\Gamma = 6A_g + 8B_{1g} + 7B_{2u} + 7B_{3u} \qquad 3\text{-}6)$$

Since the excitation fields are $E_y \; and \; H_z$, we have both $\varepsilon_{yy} < 0 \; and \; \mu_{zz} < 0$ .The reason that we have a structure like this is that we are interested in complementary metamaterial with no dielectric substrate. Conventional metamaterials need a dielectric substrate to be mechanically mountable which is a disadvantage for any S band HPM applications, because dielectrics tend to build charge and suffer from breakdown in such environments.

Figure 3-16 shows the constitutive electromagnetic parameters of the proposed metamaterial.

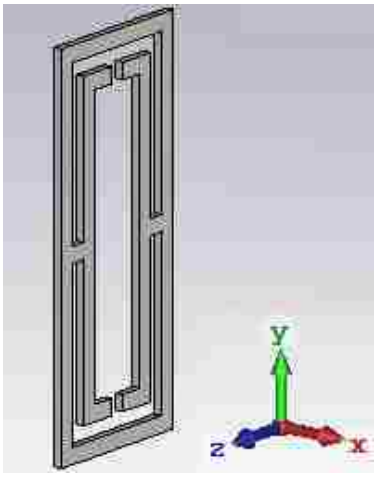

Figure 3-15: One sheet of isotropic negative index metamaterial.

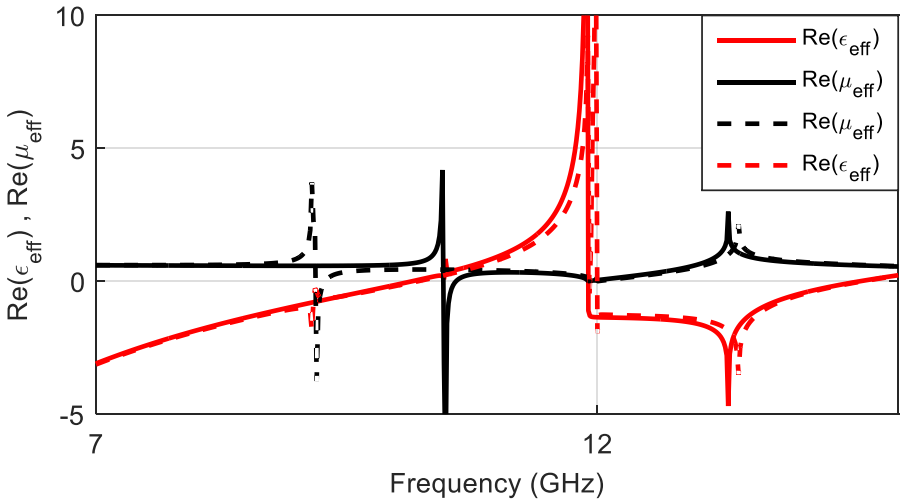

Figure 3-16: Electromagnetic constitutive parameters of the proposed metamaterial.

Considering the results in Figure 3-16, now it is time to bring a negative permeability within the frequency region as its negative permittivity, so two dissimilar metamaterials will be adjusted like in Figure 3-17.

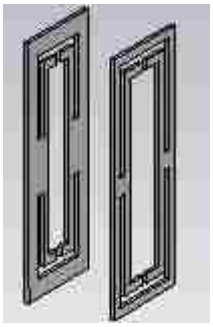

Figure 3-17: Isotropic negative index metamaterial.

To the author's knowledge, it is the first time that an isotropic (no Magneto-electric effect) negative index metamaterial, with simultaneous negative permeability and permittivity has been proposed. This type of metamaterial cam be used in a lot of high power microwave applications, especially in new HPM source design.

4 Chapter 4 Multi-Beam Backward Wave Oscillator

4.1 Introduction and Motivation

One of the main challenges in designing vacuum electron devices is their size and efficiency. Therefore, improving vacuum device efficiency and decreasing their size has been a hot topic for research.

As it was explained in previous chapters, metamaterials' unique electromagnetic properties, such as the negative refraction index, reversed Doppler effect, reversed Cherenkov radiation (RCR) have brought a lot of attention to their application in antenna design, cloaking, terahertz radiation accelerator applications, coherent microwave generation and metamaterial-based vacuum electron devices [49], [50], [51], [52], [53].

This chapter focuses on investigating metamaterial applications in vacuum devices for microwave power generation. A new metamaterial design is provided based on group theory. The designed metamaterial couples with the electron beam passing through it and RF power is generated. The device behaves like a slow wave structure (SWS) BWO.

Particle in Cell (PIC) simulation is used to simulate the designed BWO performance. This work shows that the designed BWO oscillator with an applied voltage U = 440 kV, an electron beam current I= 250A $\times$ 4 = 1 kA, and a static magnetic field B = 1.5 T generates radiation power of P = 120 MW, with TM_{01} mode at a frequency f = 3.4 GHz, and efficiency η = 23%

4.2 MTM Design

The use of metamaterials for designing microwave generation vacuum sources has been reported in literature [36], [49], [54], [55], [56], [57], [58].

In [53], a metamaterial-based microwave generator BWO, with a complementary-SRR (CSRR) to provide negative permittivity in combination with a TM mode to interact with a high-power electron beam was designed. The reported simulations show that after 250 ns, the output power of BWO is 5.75 MW with an efficiency of 14%. So, the proposed metamaterial based BWO [53], suffers from both low output power <6MW, and very slow growth response (250 ns)!.

The reported O-type high power microwave oscillator in [58], was based on a similar idea of a microwave structure with a below cut-off circular waveguide and with loads of oppositely oriented split ring resonators. They have reported that for an applied electron beam voltage of 400 kV, an electron beam current of 4.5 kA, and a guide axial magnetic field 2T, the output power of 240 MW with an efficiency of 15% can be achieved. Also, the response time for this was 10ns which is much faster than the 250 ns response in [53]. However, the problems with this design are: *first*, the output mode is a TE_{21}- like hybrid mode, which is a not a pure and practical mode and *second* it has a very low efficiency.

In [57], a S-band metamaterial-based BWO is presented. The simulated results reported show that for an electron beam of 240kV and 35A current, an efficiency up to 90% with the peak output power of 4.5 MW can be achieved. It was also reported that the maximum output saturated peak power is more 12 MW with the electronic efficiency of 65%. The presented design by [57], has a good efficiency but still suffers of both low output power ($\sim 10MW$) and very slow response time (100ns).

Here, in this chapter, the goal is to design a fast growth response, efficient BWO which optimizes electron beam coupling to a metamaterial slow wave structure through multi-beam interaction. It is amenable to the design of a BWO which is not volumetric and at the same time can increase electron beam interaction with SWS loads. A specific structure was developed for this purpose comprising a number of MTM metallic plates that have periodicity in the axial direction and are repeated in the azimuthal coordinate. Unlike [53], [58] and [57] the metamaterial based BWO in this dissertation is not based on a cut-off waveguide and the metamaterial structure designed is are responsible for providing both negative permittivity and permeability at the same time. Simulations show that the designed four beam BWO with an electron beam of 440 kV and current of 250*A* per each beam (1 kA in total) generates 105 MW with a rising time about 50ns. At UNM experimental equipment, SINUS-6 electron beam accelerator produces short pulses (no longer than few ns) which limits us to design fast response devices.

Here, a multi-beam interaction being introduced for the first time for the design of a Backward wave oscillator that interacts with a metamaterial, and increases the output peak power and efficiency.

As explained in previous chapters, metamaterials are artificial periodic structures, which support reversed Cherenkov radiation and backward wave propagation. One of the exotic properties of MTM loaded waveguide is decreasing the phase velocity in the guiding structure. This property, in addition to negative refractive index, makes MTMs interesting candidate to investigate their interaction with electron beam to generate reverse Cherenkov radiation. Since we are interested in high power microwave (HPM) generation, conventional metamaterials with dielectric substrate are not suitable for HPM applications.

First because dielectrics tend to build a charge and suffer breakdown, which leads to heating and melting downs in such environments. Second, thin metamaterial metallic patches (~0.01mm) are deformed in HPM environments. So, the proposed metamaterial here is all-metallic with more than 1mm thickness.

In chapter 3, an all-metallic anisotropic metamaterial which has a refractive index which was discussed. In this chapter, the focus is on the dispersion characteristics of a circular waveguide, loaded radially with twelve metamaterial plates which are periodic in axial direction.

Each unit cell is a pair of two parallel plates, with one plate providing a negative ε and the other providing negative μ. Each unit cell pair, is connected to the inner wall of the circular waveguide and is repeated in the azimuthal direction with an angle of ninety degree . So there are four pairs of metamaterial in each unit cell, and the structure also has periodicity in axial direction. The unit cell configuration is shown in Figure 4-1. Table 4-1 presents the physical dimension of designed metamaterial.

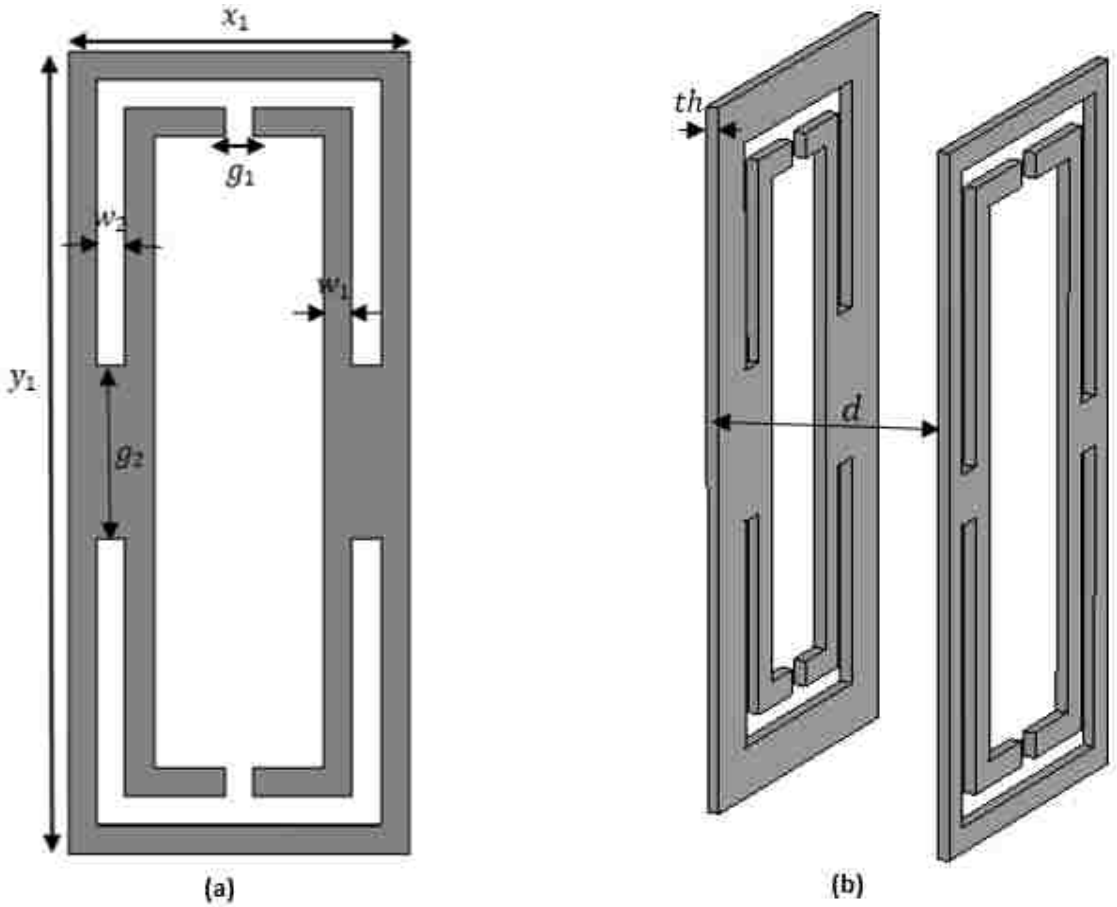

Figure 4-1 Geometry of designed metamaterial (a) one plate dimensions (b) parallel plate configuration.

Table 4-1 Dimension of Designed Metamaterial.

	x_1	y_1	g_1	g_2	w_1	w_2	th	d
Plate 1 (mm)	16	24	1	6	2	2	2	5
Plate 2 (mm)	16	24	1	10	1	1	2	5

The full wave CST Microwave Studio solver(MWS) was used to simulate the eigenmodes and then calculate the dispersion diagram of the structure. One-unit cell of a coaxial waveguide loaded with designed metamaterial is shown in Figure 4-2.

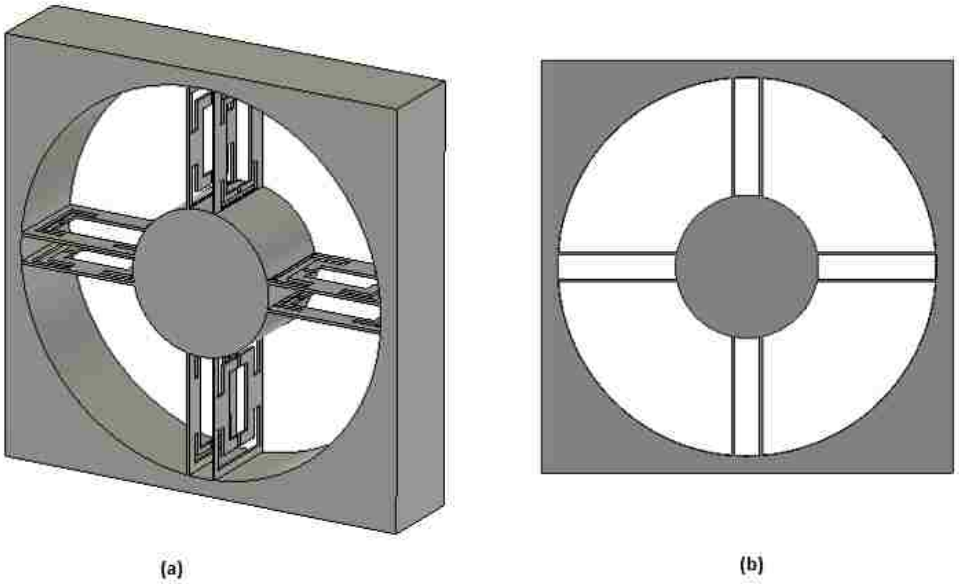

Figure 4-2 (a) One unit of MTM loaded circular waveguide (b) Dimensions $r = 35\ mm$.

The eigenmode solver enforces a phase advance $\Delta\varphi$ across the structure period in axial direction of propagation. Then it repeats the simulations for different phase advances to find the dispersion loaded waveguide. The dispersion diagram gives frequency vs wavenumber behavior for different modes of system.

The cutoff frequencies of the first three modes in a circular waveguide with radius $r = 35\ mm$ is presented in Table 4-2.

Table 4-2 Cutoff frequencies of coaxial waveguide with $r_{out} = 35\ mm$.

Mode	Cut-off Frequency
TE_{11}	2.5 GHz
TM_{01}	3.28 GHz
TE_{01}	5.2 GHz

The simulated dispersion diagram of the first two lowest modes are calculated and shown in Figure 4-3. In addition to the dispersion diagram, the beam line of $\omega = k_z v_0$ is included in the dispersion diagram to show the interaction point.

Here $v_0 = \beta_A c$, with c being the speed of light. The diagram shows that electron beam line interacts with the backward wave at f = 3.4 GHz. For calculating the electron beam line, first the value of the electron rest mass ψ_0 is calculated the from equation (4-1).

$$\psi_0 = \frac{m_0 c^2}{e_0} \tag{4-1}$$

where $m_0 = 9.109 \times 10^{-31} kg, c = 3 \times 10^8 \, {}^{m}/_{S}, e_0 = 1.602 \times 10^{-19} coulombs$. This results in a value of $\psi_0 = 511 \, Kev$.

The relativistic factor γ_A can be calculated [59] from equation (4-2).

$$\gamma_A = 1 + \frac{\psi}{\psi_0} \tag{4-2}$$

If the applied voltage ψ is chosen to be 440 Kev then $\gamma_A = 1.8598$. Using the γ_A value, the velocity of electron beam to the speed of light is calculated through equation (4-3) . Which in the case of our simulation $\beta_A = 0.84$.

$$\beta_A = \frac{\sqrt{\gamma_A^2 - 1}}{\gamma_A} \tag{4-3}$$

The CST eigenmode solver shows that the group velocity, $v_g = \frac{\partial \omega}{\partial k}$ is less than zero and is about -0.2c for frequencies above cut-off of TM_{01} mode (cutoff the TM_{01} mode in the empty rectangular waveguide is 3.2 GHz.

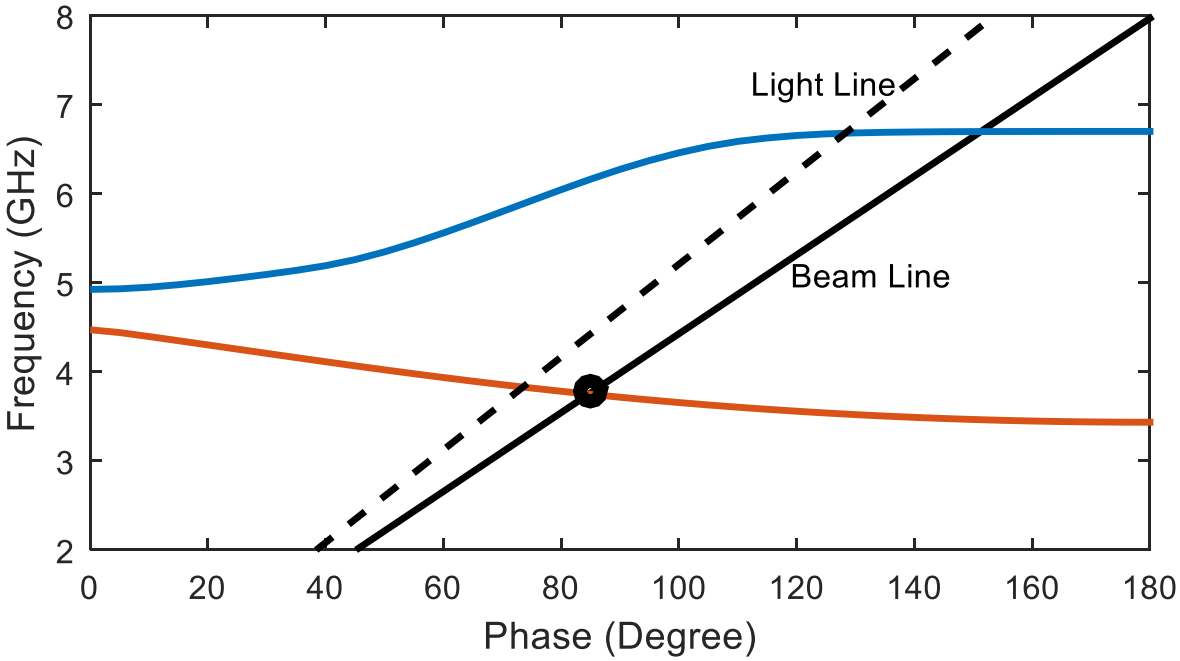

Figure 4-3 Dispersion diagram for the designed metamaterial for the first two modes with the light line (dashed) and the beam line (solid).

It is informative to investigate the various field modes to understand the beam interaction better. Figure 4-4 shows the electric field distribution for a phase advance of 85 degrees, which shows the interaction points for the modes with the beam line. The electric field is a TM-like mode for the negative group velocity mode shown in Figure 4-3. So, the electric field that electron beam experiences when passing through the structure, (emitter diameter is 2mm) is TM like mode.

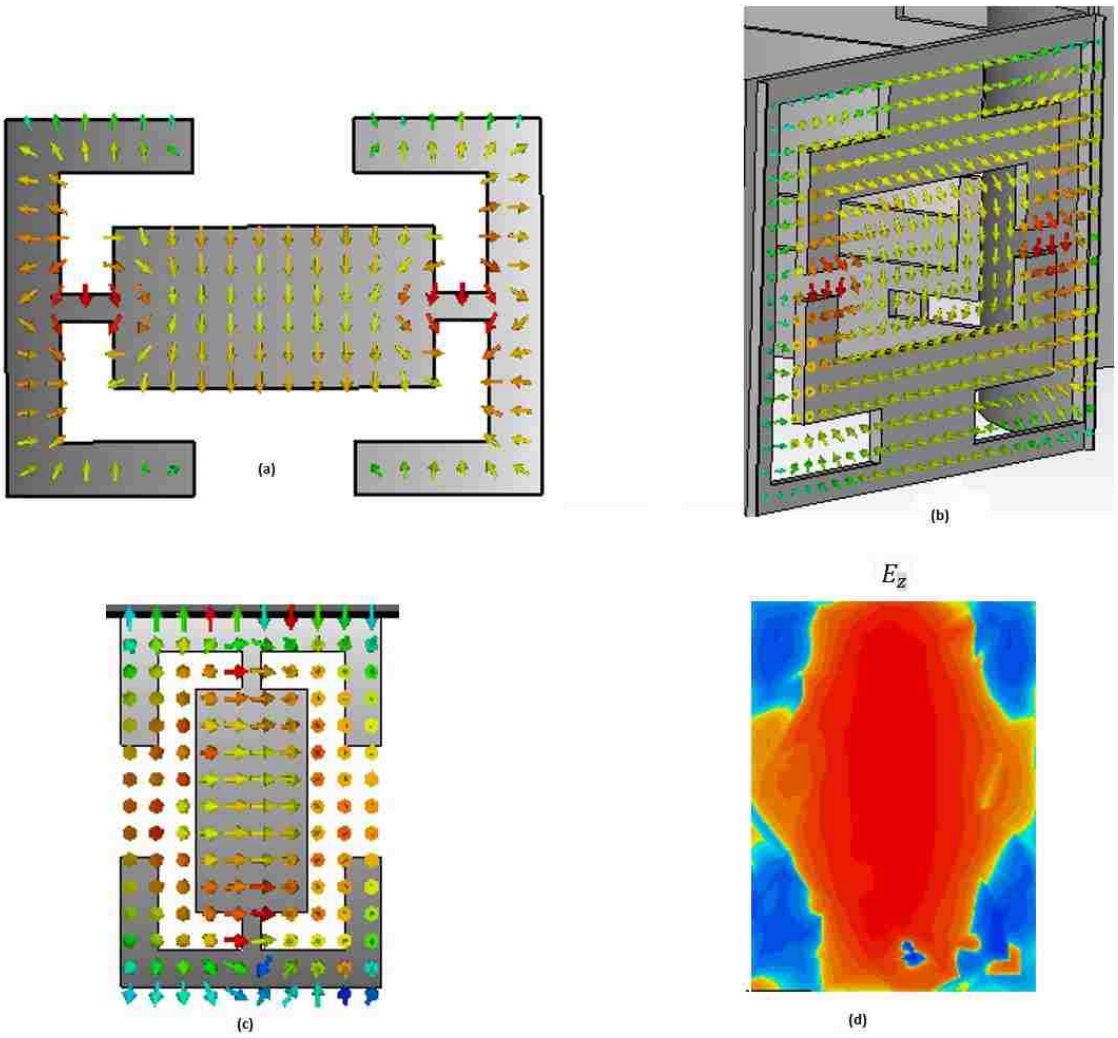

Figure 4-4 Electric Field Distribution between metamaterial plates from different angles.

To understand the backward propagation nature of the structure, it is instructive to consider the wave propagation in a cold test (without electron beam presence).

4.3 Theory of Electron Beam Interaction with metamaterial Waveguide

To understand the metamaterial-based BWO performance, some parameters are defined to further explain their interaction.

The coupling impedance measures the interaction level between the electron beam and an EM wave.

$$Z = \frac{E_z^2}{2k_z^2 P} \tag{4-4}$$

where E_z is the axial component of the electric field in beam position (between plates), k_z is the wavenumber, and P is axial power flux.

$$P = \oiint_S E \times H^* \tag{4-5}$$

S is the area of a waveguide cross section perpendicular to direction of propagation.

Another important parameter to calculate is the start current for oscillations to occur. In conventional BWOs such as rippled wall BWOs, when a beam current is above the start current (I_{st}), the BWO starts to generate microwave RF output with zero input signal (from noise). Start current is a function of coupling impedance, mode of interaction, geometry and beam energy. In [59 MIT] a method has been developed to calculate the start current for a TM mode interaction case, which is talso he case for the design in this dissertation. Pierce's theory presented in [33] only gives accurate results when the group velocity is not very low.

$$I_{st} = 4U_0 \frac{(CN)_{st}^3}{ZN^3} \tag{4-6}$$

U_0 here is the beam energy, N is the length of the structure in wavelengths, $N = L/\lambda_z$ with λ_z the wavelength, L the total length of BWO, and C the Pierce parameter calculated by equation (4-7).

$$C^3 = \frac{I_0 K}{4U_0} \tag{4-7}$$

Z in the above equation is the interaction impedance of the structure, and I_0 is the beam current. Using [33], $(CN)_{st}$ is 0.314. Generally, $3 \times I_{st} < I_{beam} < 7 \times I_{st}$ result in the best

performance for the proposed BWO. If the beam current is increased beyond the $7 \times I_{st}$, the output power will be auto modulated.

4.4 Hot Test Particle-in-Cell Simulations

This section is dedicated to CST Particle in Cell (PIC) simulations carried out to investigate the performance of the designed MTM-loaded BWO for power generation. Figure 4-5 shows the proposed design for the metamaterial-based backward wave oscillator (MTM BWO). The BWO is designed to work in the S-Band and at 3.4 GHz. The designed BWO consists of four pairs of parallel metamaterial plates placed inside a circular waveguide with a periodicity in the axial direction. The schematic of the structure for one period was shown in Figure 4-2. The schematic of the entire structure is presented in Figure 4-5.

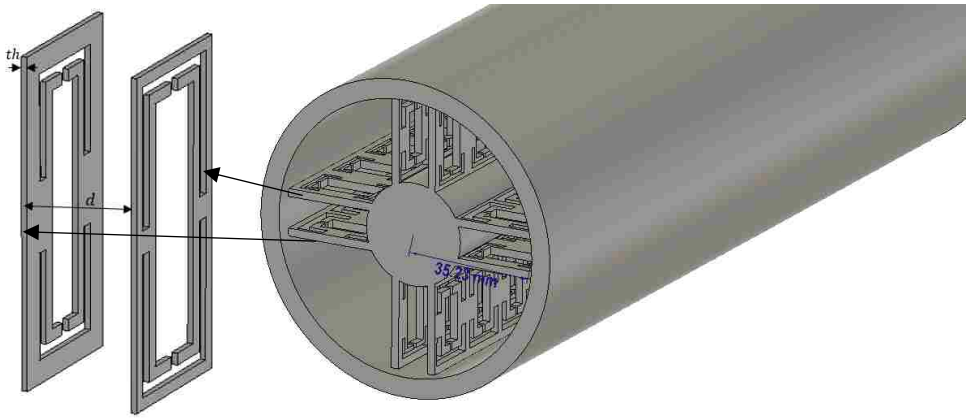

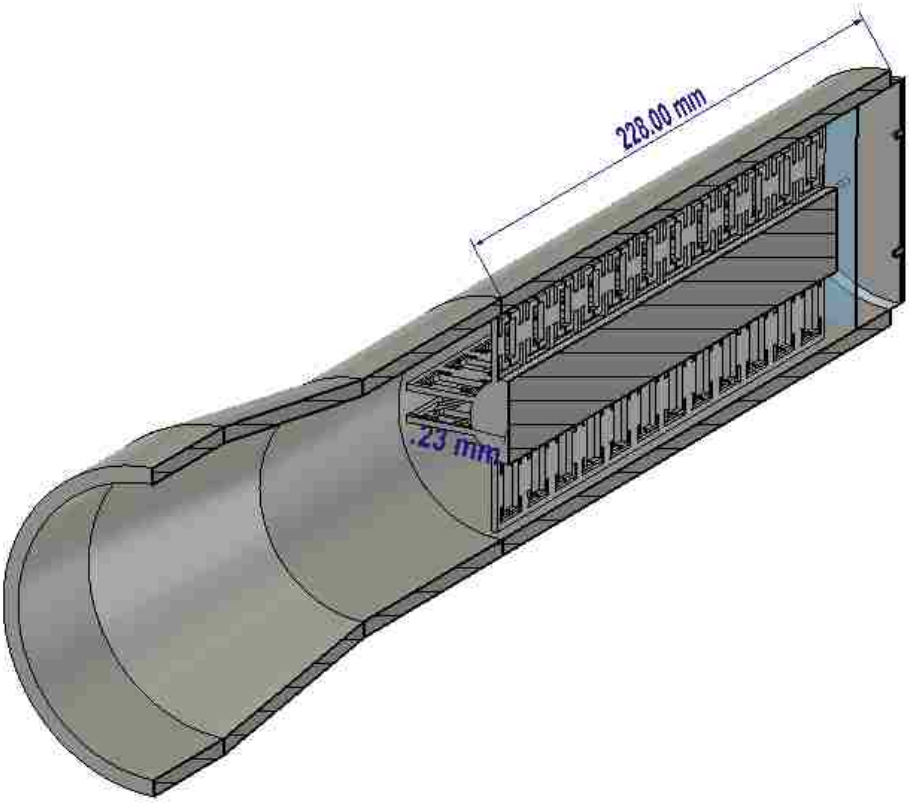

Figure 4-5 Schematic of one period of MTM-BWO and Schematic of the BWO structure.

The resonance frequency of the metamaterial is tuned to be above the cut-off frequency of a TM mode in the circular waveguide. The period of structure is 16 mm in the axial direction. The metamaterial plate thickness is 2mm and the BWO waveguide radius is 35 mm. Figure 4-5 c shows the entire BWO structure, including the output guiding part. As it can be seen the length of the slow wave structure is 228 mm and the length of the structure including the output ports is 420 mm. As it was explained in Figure 4-3, the CST eigen solver has been used to generate the dispersion diagram and the 3D electric and magnetic field vectors, to predict the BWO performance. Both the beam line $\omega = k_z v_0$ and light line in $\omega = k_z c$ is shown in Figure 4-3 Calculations showed $v_0 = 0.84c$ which is the velocity of 440 keV electron beam. The structure supports one left TM like ($H_z \approx$

0 $on\ axis$), handed propagating mode ($v_g v_{ph} < 0$). The electron beam line is supposed to be interacting with the mode.

4.5 Particle-in-Cell simulation (PIC)

The PIC solver (CST Particle Studio), was used to evaluate performance of the proposed BWO. A variable current of 800A, 1kA and 1.2 kA (200, 250 and 300 A per each beam), and a 440 keV electron beam, with a cathode radius of radius 1.1 mm, were used for the simulations. The electron beam emission is based on a DC electron beam which the electron beam current rise time is 1ns. A confining static magnetic field of 1.5T is used to keep the electron beam moving in the axial direction.

Figure 4-6 shows the radiated output power (105 MW) versus time for a the designed BWO, with a total current of 1kA.

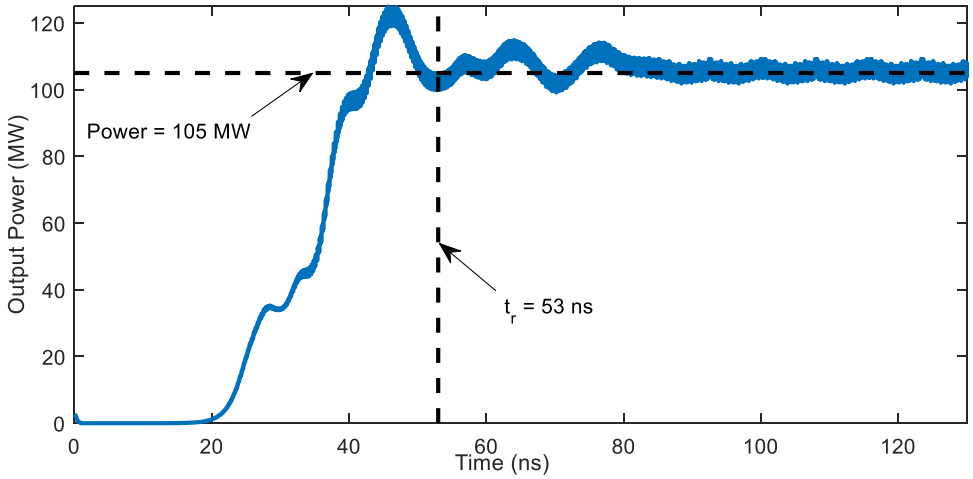

Figure 4-6 Output Power for a 1kA proposed BWO.

It can be seen in Figure 4-6, that the BWO reaches a stable power of 105MW after 53 ns. Also in Figure 4-7, the Fourier transform of the output electric field TM_{01} mode is presented. The output signal has a clear frequency response oscillating at 3.4 GHz.

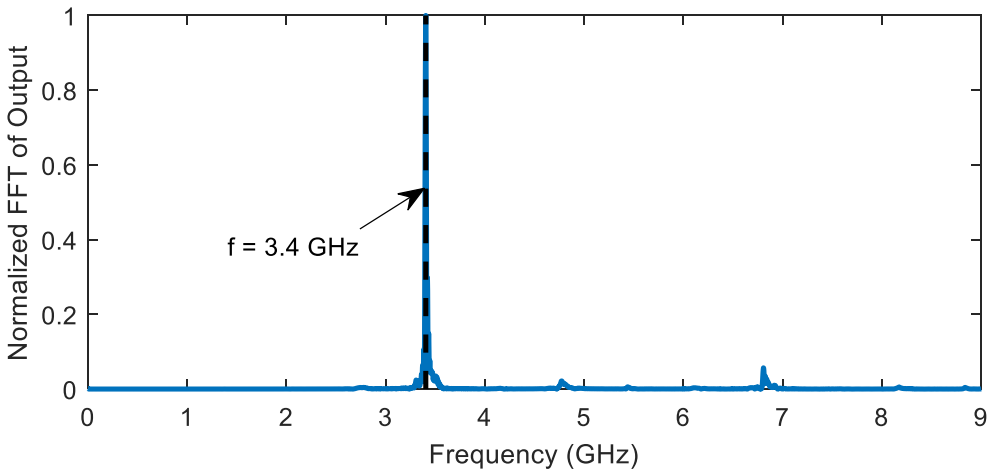

Figure 4-7 Fourier transform of output electric field TM_{01} mode.

Figure 4-8 shows the output port modes. The TM_{01} is the dominant mode.The rest of the modes are not excited and are not coupled to the electron beam.

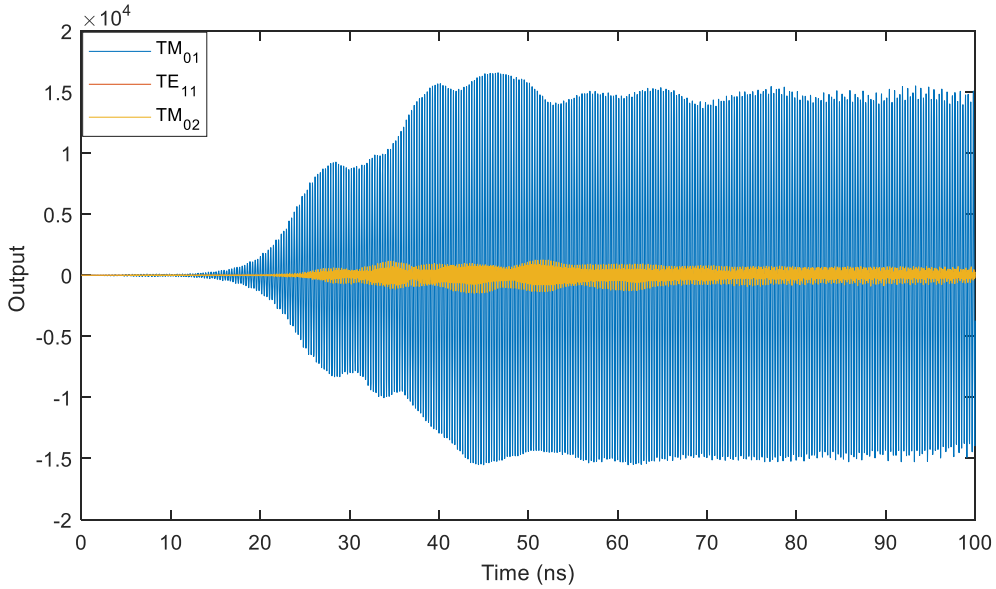

Figure 4-8 output port signal modes.

Also the electric field distribution along the BWO confirms how the TM_{01} is generated at the output port.

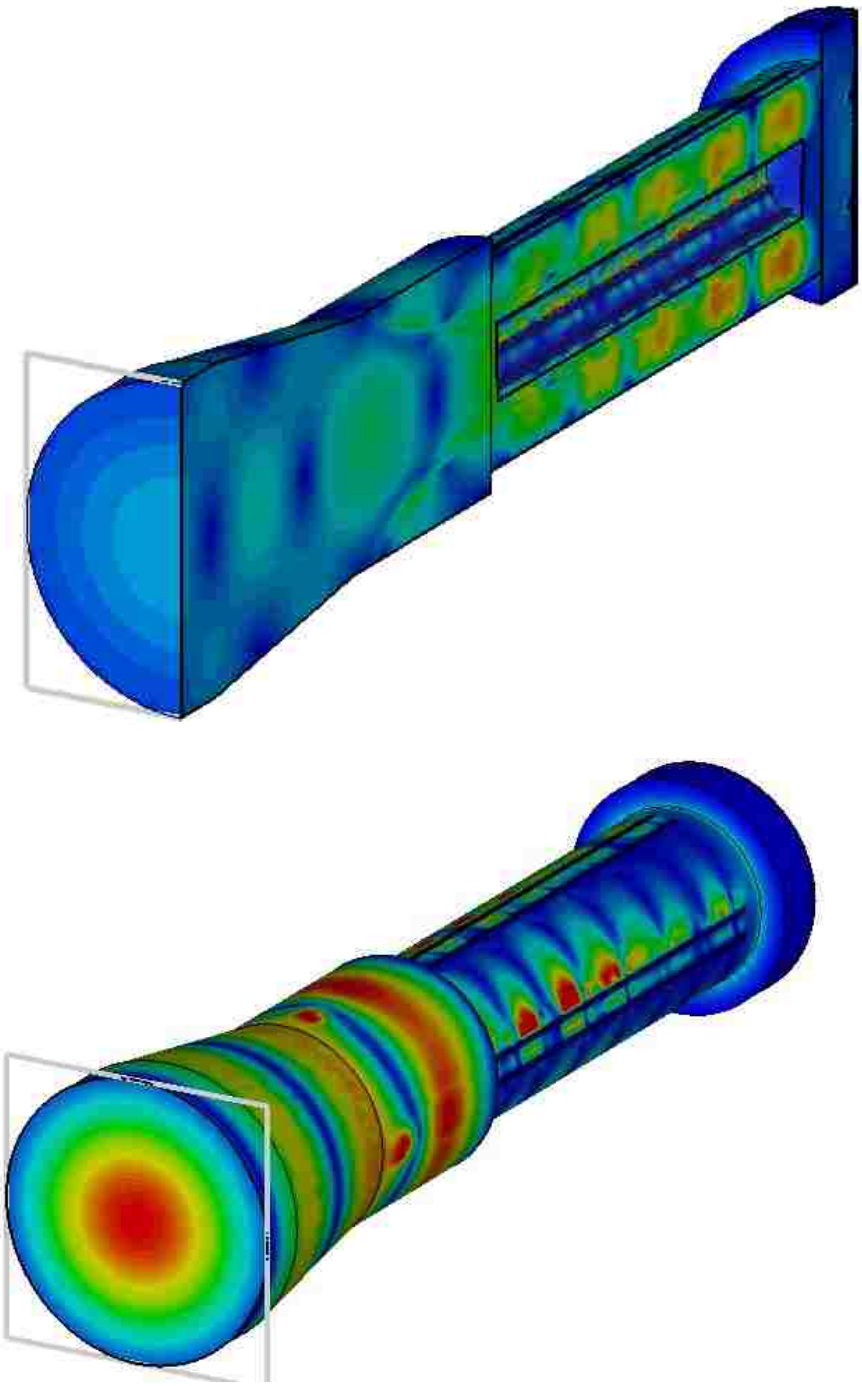

Figure 4-9 Electic field distribution along proposed BWO and output TM_{01} mode.

The PIC phase space plot of structure is shown in Figure 4-10 at t = 10ns, t = 30ns and t = 55 ns, respectiively. The phase space plot helps to visualize the absolute energy of

all particles along the BWO structure (phase space vs spatial coordinate). The phase space plots demonstrate how electron bunching form as time passes.

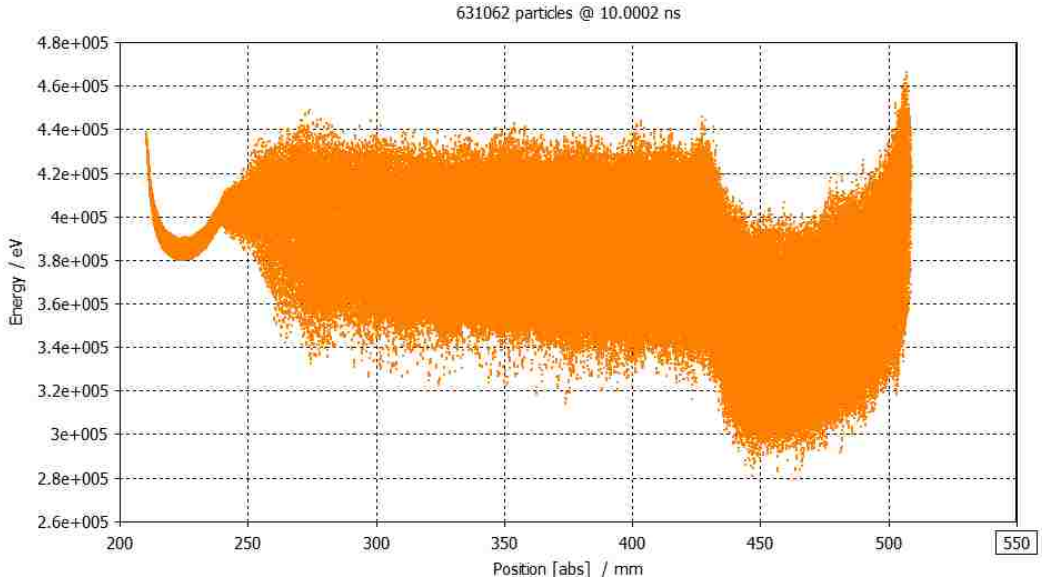

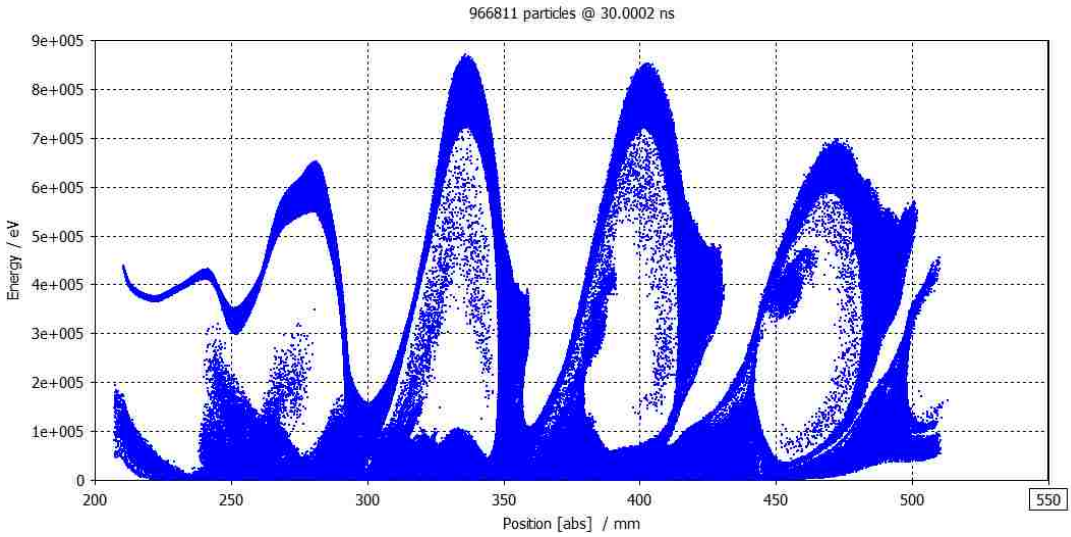

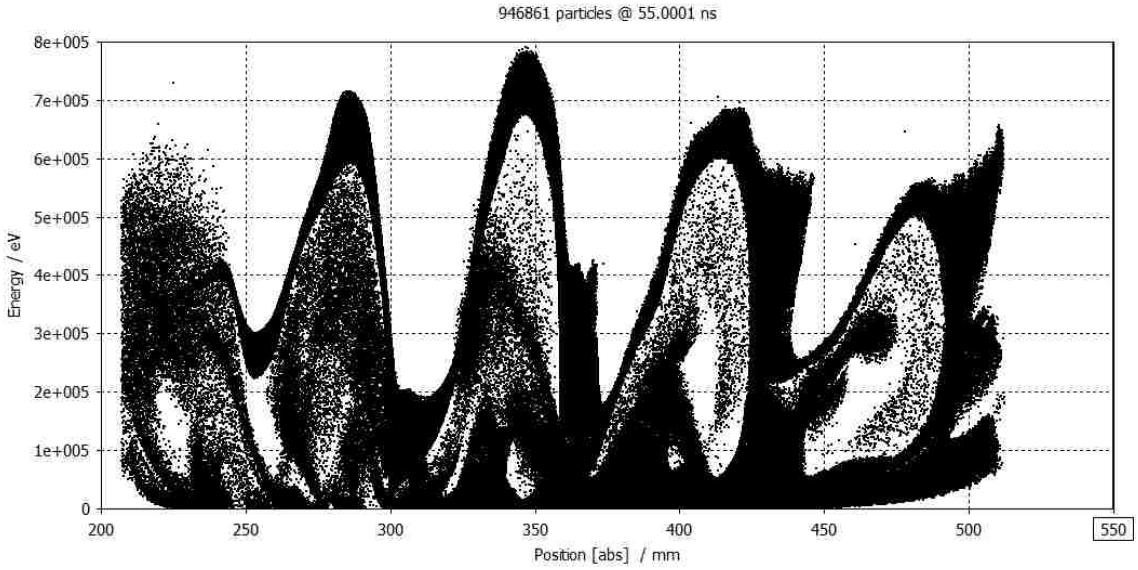

Figure 4-10 PIC phase space plot of electrons at a) t = 10 ns b) t = 30 ns c) t = 55 ns

4.6 Efficiency

For the proposed BWO, efficiency is an important parameter to be reported. The efficiency can be obtained by dividing the average steady output power by the electron beam DC input power. In the proposed BWO, the output power of 105 MW is generated from four electron beams, each with 250A current and 440 keV voltage. Therefore, the efficiency of the proposed BWO is 23.8% which is high in compare to what previously has been reported in literature.

4.7 Conclusion

In this chapter, a novel multi-beam metamaterial-based backward wave oscillator has been presented for the first time. First the CST eigenmode solver is used to show that the designed metamaterial supports the negative index propagation. The PIC solver was used to evaluate the performance of the BWO for generating power from four electron beams of total 440 keV and 1kA current. Simulations confirmed that 105 MW output power with an efficiency of 23.8% can be generated.

5 Chapter 5 Power Combiner and Power Splitter

5.1 History of Power Combiner

Most dangerous explosive materials, both toxic and radioactive, contain nitrogen salts with resonant absorption lines in the frequency range 0.3-10 THz. Therefore, there has been growing interest in remotely detecting such materials by observing the spectrum of reflected signals when the suspicious material is interrogated by THz radiation. Practical portable THz sources available today generate only 20–40 mW output power. This power level is too low to interrogate suspicious material from a safe distance, especially if the material is concealed. Hence, there is a need for sources that can provide greater power in the THz spectrum. Generating and extracting high output power from THz sources is complicated and inefficient. The efficiency of vacuum electronic microwave sources is very low when scaled to the THz range and THz sources based on scaling down semiconductor laser sources have low efficiency as well, resulting in the well-known "THz gap." The reason for such low efficiencies for both source types is material losses in the THz band. In this chapter, an efficient power combiner is described that is based on scaling to higher frequencies a microwave combiner that increases the output power in the THz range of interest in simulation studies. The proposed power combiner not only combines the THz power output from several sources, but can also form a Gaussian wavebeam output. A minimum conversion efficiency of 89% with cophased inputs in a lossy copper power combiner and maximum efficiency of 100% in a Perfect Electric Conductor (PEC)-

made power combiner were achieved in simulations. Also, it is shown that the TE_{01} output mode is a reasonable option for THz applications due to the fact that conductive loss decreases for this mode as frequency increases.

5.2 Power Combiners

During the last decade, there has been tremendous interest in the remote detection of dangerous materials such as explosives, both toxic and radioactive. Explosive materials contain nitrogen salts in their structure with resonant lines of absorption in the frequency region of 0.3–10 THz [60]. In this frequency range materials such as skin, paper, and plastic, which can be used to conceal explosive devices, are transparent. This fact motivates researchers to study the reflected spectrum of suspicious materials illuminated by a THz source to detect explosives.

The frequency range 0.3–10 THz is located between the microwave and infrared portion of the electromagnetic spectrum. The efficiency of both microwave and semiconductor laser sources drops drastically when scaled to the THz range, forming the well-known "THz gap" where available sources generate output power on the order of only a few tens of milliwatts [61]. This power level is insufficient to detect explosive material from a safe distance, especially if they are concealed. Short range screening, such as at airports, is the only practical application of such low power sources.

Reports show that some high-power THz sources do exist, but their size is huge and they are neither portable nor practical. A free electron laser [62] reported by the Institute of Nuclear Physics (Novosibirsk, Russia) generates an average power of 0.5 kW; however, it is as large as a building, housed in a large high bay facility. In addition to that, a gyrotron with pulsed magnetic field operating in a single 50 μs pulse with output power 1.5 kW [63]

has been reported by the Institute of Applied Physics (Nizhny Novgorod, Russia). This gyrotron requires a cryomagnet and a diamond window, and including its power supply is about $2m^3$ in volume and not portable.

The output power level from a single THz source is limited by material losses in the THz frequency regime. Therefore, if it is desired to generate power greater than the power generated from a single THz source, combining the beams from the output of several THz sources can be a solution. Increasing the output power of a pulse with Gaussian distribution is of significant importance to many applications, both in the microwave and THz bands [64], [35]. Using the power combiner approach can lead to output powers from vacuum electron sources on the order of a few watts, which can be used to remotely detect explosive targets from a safe distance, even when they are concealed [60].

It has been previously reported in the literature [65], [66], [67] and [68]. that combining the power from a number of parallel short pulse, high power microwave oscillators connected to a single pulser results in coherent summation of power if the phase difference between the sources is less than 25%; this requires a pulser with a very fast rising voltage pulse. In addition, an experimental study verified that two relativistic backward wave oscillators (RBWOs) working at gigahertz frequencies with gigawatt output power can be summed [67], [68]. The coherent summation of fields radiated by their horn antennas was verified by imaging the expected interference pattern using a neon bulb array. Also, in [69], it was demonstrated that by dividing the driving voltage pulse across several parallel channels equipped with independent cathodes, four synchronized superradiant sources in the form of a 2D array can be achieved which can generate fields of extremely high intensity.

In this chapter, a power combiner is proposed for THz frequencies. The proposed power combiner comprises N rectangular waveguides operating in their dominant TE_{10} mode. The N rectangular waveguides' outputs are formed in a circular configuration. The proposed power combiner not only combines the THz output sources and increases the overall power output, but also converts the input mode from each of the N sources to a more desirable overall output mode. This article is organized as follows. Section II is devoted to describing the proposed power combiner configuration and theory in detail. CST Microwave Studio is used to perform electromagnetic simulations and the results of simulations of the power combiner are presented and analyzed in Section III. Finally, the conclusions are presented in Section IV.

5.3 The Power Combiner Design

The proposed THz power combiner uses N rectangular waveguides, each operating in the dominant TE_{10} mode. Each waveguide is driven by a THz source. The configuration of the power combiner is shown in Figure 5-1. As can be seen from the Figure 5-1, N sectorial single mode rectangular waveguides enter into a coaxial channel so that the sectorial waveguides produce a solid circle filling the space between electrodes of the coaxial channel. We choose the gap between the coaxial surfaces so that only azimuthally uniform modes with the minimal radial index can exist. The cross section of the inner electrode of the coaxial geometry is gradually tapered until it disappears, resulting in a cylindrical waveguide output. Depending on the orientation of the rectangular waveguide, the output mode can be the TM_{01} mode for the case when the input electric field of the rectangular waveguide is oriented in the $\vec{r}$ direction (radial), or can be the TE_{01} mode when the input electric field of the rectangular waveguide is oriented in the $\vec{\varphi}$ direction

(azimuthal). It should be emphasized that, even though the cylindrical output waveguide is oversized, the output is single mode due to symmetry.

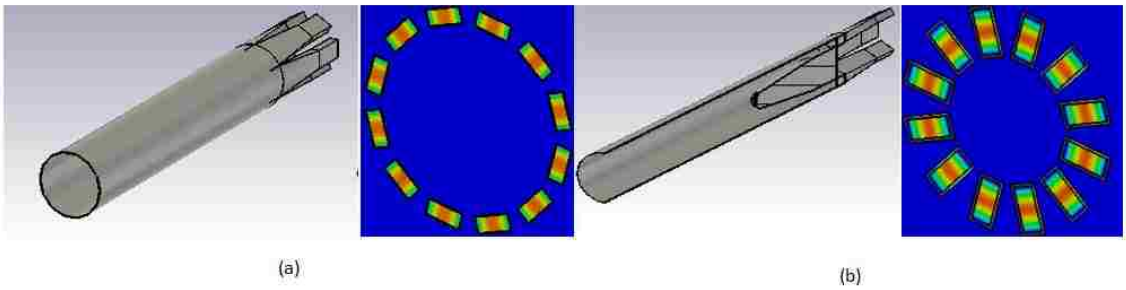

Figure 5-1 The structure of the power combiner; a) radial TE_{10} excitation; b) azimuthal TE_{10} excitation.

In principle, high efficiency combining in such a multimode power combiner is possible for perfect symmetry and absolutely identical cophased inputs of the main mode and compensation of parasitic modes; however, this is unrealizable in practice. At the same time it is pertinent to note that it is possible to overlap the feeding waveguides to achieve more uniform electromagnetic fields at the input port of the combiner. More convenient combiners that can be used for the THz region are described in the next Section, where we also intend to use overlapping input waveguides. In this chapter we use a coaxial design for a power combiner that excludes exciting modes with radial indices n>1.

5.4 Results

This Section is dedicated to investigating the effects of different parameters on power combiner performance.

5.4.1 The Effect of the Number of Inputs on Combiner Performance

In order to investigate the performance of the power combiner in detail, we first study the effect of the number of inputs on the power combiner efficiency. The power combiner in this section has the TM_{01} mode as output with the input electric field of the rectangular

waveguide oriented in the $\vec{r}$ direction; the electric field is radial. For the electric field at the combiner output to be radial the rectangular waveguides themselves (longer dimension of waveguide "a") must be oriented in the $\vec{\varphi}$ direction.

For the THz studies presented in this article, the power combiner has parameters $a = 0.508$ mm, b = 0.254 mm (standard WR-2 waveguide dimensions), and its operating frequency is from 0.325-0.5 THz with cutoff frequency 0.295 THz. The length of circular waveguide is chosen to be $15r_{\mathrm{cw}}$ and the length of the tapered inner electrode of the coaxial is chosen $1.67r_{\mathrm{cw}}$, where r_{cw} is the circular waveguide radius at the output.

For the three different cases $N = 6,9,12$ where N indicates the number of rectangular waveguide inputs and each is excited with the dominant TE_{10} mode with cophased radial electric field, the input power P = 0.5 W. The efficiency of the power combiner can be calculated through $\eta = P_{out}/\sum_N P_N$.

It needs to be emphasized that, as mentioned earlier, the output waveguide is an oversized waveguide. For example, for the $N = 6$ case the circular waveguide radius is $r_{\mathrm{cw}} = 0.91$ mm at frequency $f = 420$ GHz (the frequency that the calculation results are presented in). 18 modes can propagate in this waveguide (the highest feasible mode is the TE_{32} mode with cutoff frequency 419 GHz). For the $N = 9$ case $r_{\mathrm{cw}} = 1.3$ mm and it can support 30 modes (the highest feasible mode is the TE_{33} mode with cutoff frequency of 416 GHz). For the $N = 12$ case $r_{\mathrm{cw}} = 1.75$ mm and in this waveguide 52 modes can propagate (the highest feasible mode is the TE_{63} mode with cutoff frequency 416 GHz). In all three cases the TM_{01} mode is the only output mode because of symmetry. As was explained earlier, the dominant mode in radial excitation is the TM_{01} mode; however, part of the power also couples to the next higher mode, which is the TM_{02} mode.

Figure 5-2 shows the output power efficiency for the TM_{01} mode. It can be concluded that, the greater the number of input waveguides with identical power, the greater will be the output power in the TM_{01} mode. This, however, is not correct because the greater the number of inputs N, the larger will be the cross section of the combiner and the greater will be the number of modes that can be excited with less efficiency for the formation of the dominant mode. Using the information in Figure 5-2 the maximum efficiencies for power combining $N = 6,9,12$ inputs and related parameters can be extracted and the results are summarized in Table 5-1.

For the case $N = 6$, 98.3% of the input power couples to the output TM_{01} mode and 1% of the power couples to the TM_{02} mode.

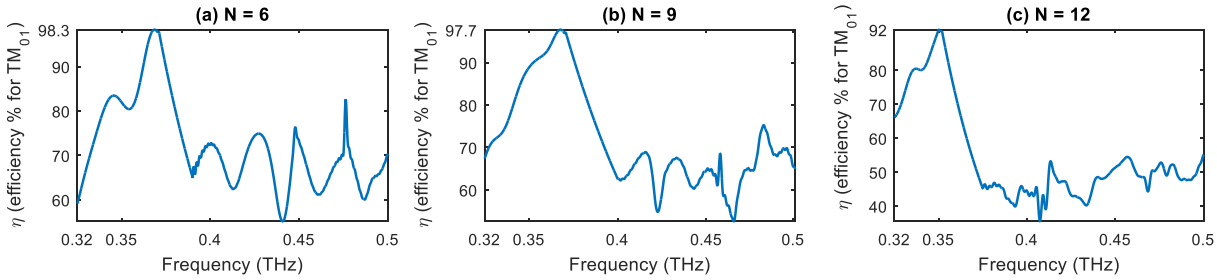

Figure 5-2 Output power efficiency for TM_{01}mode (radial inputs),a) $N = 6$ inputs; b) $N = 9$ inputs; and c) $N = 12$.

Table 5-1 The ratio of output power to radial input powers, maximum output power efficiency and corresponding frequency for N=6, 9, 12.

N	$\frac{P_{TM_{01}}}{P_{TE_{10}}}$(dB)	$\eta_{TM_{01}}$	f (GHz)
6	7.7 dB = 5.89	98.3%	368
9	9.36 dB = 8.64	97.0%	366
12	10.42 dB = 11.56	92.0%	350

When $N = 9$, 97% of the input power couples to the TM_{01} mode and 2% of the power couples to the TM_{02} mode. For $N = 12$, 92% of the input power couples to the TM_{01} mode,

6% of the input power couples to the TM_{02} mode and the rest couples to $TM_{0n}, n \geq 3$ modes.

5.4.2 Input Polarization

This portion of the work investigates the effect of excitation field polarization on the power combining efficiency. For simplicity, only results for the $N = 12$ case will be shown.

Two polarizations are investigated. In case 1,Figure 5-3(a), the input electric field is in the $\vec{r}$ direction in cylindrical coordinates while in case 2, Figure 5-3(b), the input electric field will be in the $\vec{\varphi}$ direction in cylindrical coordinates. In order to facilitate comparisons of the results for the two cases we choose as input standard WR-2 waveguide with $a = 0.508$ mm and $b = 0.254$ mm. Thus, for case 2 where the input electric field is in the $\vec{\varphi}$ direction, the coaxial-circular channel radius will be smaller and we expect higher efficiency in general. The dominant output mode for case 1 is the TM_{01} mode while for case 2 it is the TE_{01} mode.

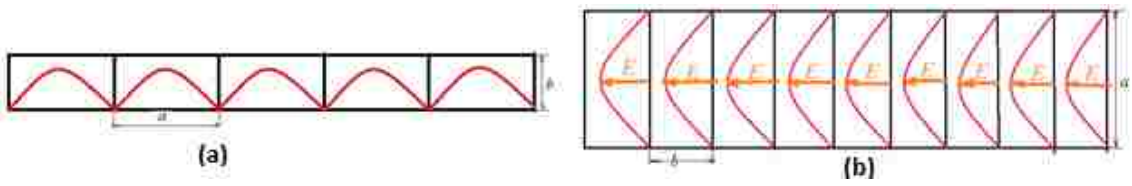

Figure 5-3 Polarization of the input signal: a) TE_{10} radial distribution; b) TE_{10} azimuthal distribution.

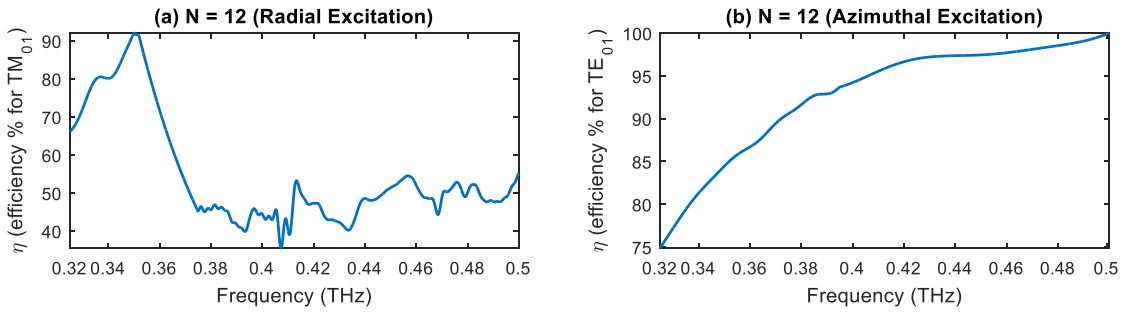

Figure 5-4 Output power efficiency with N = 12 inputs a) radial TE_{10} inputs; b) azimuthal TE_{10} inputs.

Table 5-2. The ratio of output power to input powers, maximum output power efficiency and corresponding frequency for radial and azimuthal inputs.

Excitation	**Output Dominant Mode Power**	$\boldsymbol{\eta_{TM_{01}}}$	$\boldsymbol{f}$ **(GHz)**
Radial	10.42 dB = 11.56 $(\boldsymbol{P_{TM_{01}}/P_{TE_{10}}})$	92%	350
Azimuthal	10.79 dB = 12 $(\boldsymbol{P_{TE_{01}}/P_{TE_{10}}})$	100%	500

According to Figure 5-4. and the efficiency calculations in Table 5-2, when the input electric field is in the $\vec{r}$ direction the maximum power combing efficiency is 92% and only occurs for one frequency ($f = 350$ GHz), while when the input electric field is in the $\vec{\varphi}$ direction the maximum power combing efficiency is 100% at $f = 500$ GHz and the efficiency of the structure increases with frequency and is greater than 93% from 0.38-0.5 THz, which makes the azimuthal direction input ($\vec{\varphi}$) electric field case a more reliable, stable, and broader bandwidth power combiner. The TE_{01} output mode has a very unique property, which makes it very desirable for THz applications. For the perfect electric conductor (PEC) power combiner, since for the TE_{01} mode the electric field is purely azimuthal ($E_\varphi \neq 0, E_r = E_z = 0$) on the outer wall of the circular waveguide, due to the PEC boundary condition, even E_φ, which is the tangential electric field, goes to zero on

the wall ($E_\varphi = 0$); therefore, for the TE_{01} mode, $E_{\mathrm{total}} = 0$ (on walls). As a result, surface currents will be excluded for this mode. Therefore, as frequency increases, the efficiency increases as well, while in the previous case (radial excitation, Figure 5-4), efficiency drops at high frequencies due to surface currents. For both cases the input power is the same since both cases have 12 input rectangular waveguides operating in the dominant TE_{10} mode with the same size, and therefore, the same power handling capability. Figure 5-5(a) shows the distribution of the input mode and Figure 5-5(b). shows the distribution of the output mode of the power combiner.

5.5 Power Combiner using Realistic Lossy Material

The results presented in the previous two Subsections assumed that the THz-band power combiners were constructed of PEC material. In this Subsection the results of the same power combiner performance using lossy copper material will be presented.

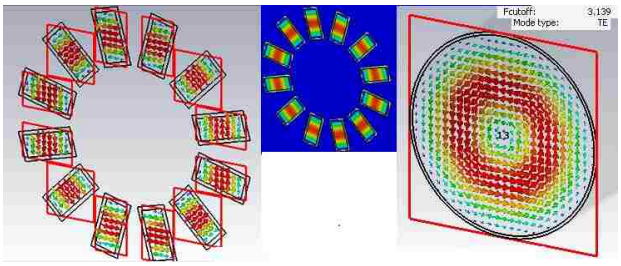

Figure 5-5 Azimuthal input TE_{10} input: a) distribution of the input signal; b) output TE_{01} mode.

Since the azimuthal TE_{10} mode input excitation showed more promising and stable results, the results here will be shown for a power combiner in the THz regime made from lossy copper with $N = 6$ azimuthal excitation inputs.

In this example, $a = 0.54$ mm and $b = 0.23$ mm (and the results are summarized in Table 5-3.). As can be seen from Figure 5-6, the maximum power combining efficiency drops to 89% for the power combiner made from lossy copper in the THz regime. Figure

5-6 also shows that as frequency increases, the efficiency of the power combiner increases. In this case, since the wall material is lossy, $E_{\text{tangential}} = E_{\varphi} \approx 0$ on the walls; therefore, the wavenumber becomes complex $\gamma = \alpha + j\beta$ and the attenuation coefficient α is no longer zero. However, since for the TE_{01} mode, $\text{H}_{\text{tangential}} = H_{\varphi} \approx 0$, the attenuation coefficient α due to conductor loss of the TE_{01} mode decreases to very small values with increasing frequency [70]. This property makes the TE_{01} mode of interest for THz application due to its low losses in the THz regime.

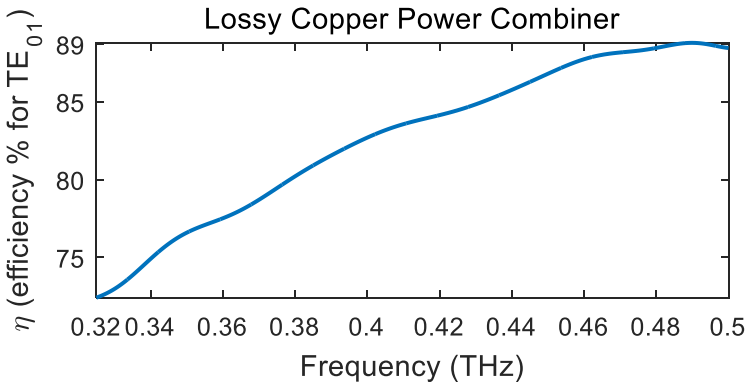

Figure 5-6 Output power efficiency for a power combiner made from lossy copper.

Table 5-3. The ratio of output power to azimuthal input powers, maximum output power efficiency and corresponding frequency for PEC and lossy copper material power combiner.

Material	$\frac{P_{TE_{01}}}{P_{TE_{10}}}$	$\eta_{TM_{01}}$	f **(GHz)**
PEC	10.79 dB = 12	100%	500
Lossy Copper	10.32 dB = 10.77	89%	500

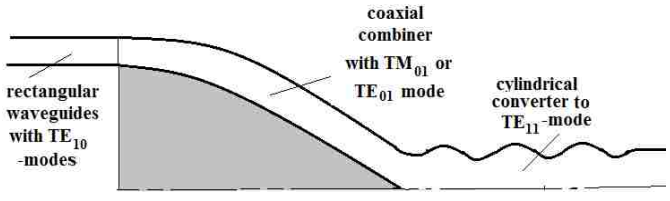

Figure 5-7 Power combiner cross section with output corrugation.

As has been shown, the TE_{01} mode is an attractive candidate for THz applications since its efficiency increases with frequency. However, there is always a risk of its conversion to the degenerate TM_{11} mode due to the fact that they have the same cutoff frequency. This problem can be easily remedied through adding corrugation to the output channel, as shown in Figure 5-7. The procedure will be explained with more details in the next Section.

5.6 Power Combiner with the Output TE_{11}-Mode

For most applications, it is preferred to have the output mode be a Gaussian wavebeam since a Gaussian beam has maximum power at the center. In order to convert the output wave to a Gaussian form and at the same time as eliminating the degenerate non-desirable TM_{11} mode mentioned earlier, a periodic corrugation as shown in Figure 5-7. needs to be added along the output cylinder. Here we describe how to convert the power combiner output to a desirable Gaussian mode. Using this technique, the output mode will be 85% TE_{11} mode and 15% TM_{11} mode that describes a Gaussian output [13]. It has already been shown [71], [72] that the TE_{11} mode can be converted from the TE_{01}/TM_{01} mode (which are the power combiner output) using a spiral sinusoidally corrugated cylindrical channel of length L in which the number of spirals $\bar{m}$ is equal to equation (5-1).

$$\bar{m} = m_1 \mp m_2 \tag{5-1}$$

where m_1 is the azimuthal index of the incident wave, m_2 is the azimuthal index of the converted wave, and the sign of $\bar{m}$ indicates a right- (+) or left- (-) handed spiral; the period d of corrugation can be calculated from equation (5-2).

$$\vec{h} = \frac{2\pi}{d} = [h_1 - h_2] \tag{5-2}$$

Where h_i is calculated from equation (5-3).

$$h_{1,2} = \sqrt{k^2 - \left(\frac{\nu_{1,2}}{R}\right)^2} \tag{5-3}$$

and h_1 and h_2 are the longitudinal wavenumbers of the converted modes, respectively. $k = \frac{2\pi}{\lambda}$ where λ is the operating wavelength, R is the average radius of the corrugated channel, and $\nu_{1,2}$ are the roots of the Bessel function for the corresponding TM(E) modes or the roots of the derivatives of the Bessel function for the corresponding TE(M) modes. The coefficient of mode conversion for the electromagnetic field is calculated from equation (5-4).

$$K_E = \sin^2(\delta L) \tag{5-4}$$

where L is the length of the corrugated channel and is chosen such that $L = \frac{\pi}{2\delta}$ [72]. The coupling coefficient for converting the TE (TM) mode to an TE (TM) mode is calculated from equation (5-5).

$$\delta_{HH}(\delta_{EE}) = \frac{l}{2R}\frac{m_1 m_2(k^2 + h_1 h_2) + \nu_1^2 \nu_2^2}{[h_1 h_2(\nu_1^2 - m_1^2)(\nu_2^2 - m_2^2)]^{0.5}} \tag{5-5}$$

where l is the amplitude of the sinusoidal corrugation. In order to convert the TM (TE) mode to a TE (TM) mode the coupling coefficient is calculated from equation (5-6).

$$\delta_{EH} = \frac{l}{2R}\frac{m_H k \bar{h}}{[h_E h_H(\nu_H^2 - m_H^2)]^{0.5}} \tag{5-6}$$

Finally, to convert an E mode to an E mode the coupling coefficient is calculated from equation (5-7).

$$\delta_{EE} = \frac{l}{2R}\frac{k^2 + h_1 h_2}{[h_1 h_2]^{0.5}} \tag{5-7}$$

In the designed power combiner, the azimuthally symmetric TE_{01} mode ($m_1 = 0$) needs to be converted to the asymmetric linearly polarized TE_{11} mode; therefore, the coupling coefficients are $\delta_{TE_{01}\to TE_{11}} = \frac{l}{2R}\frac{v_{01}v_{11}^2}{\sqrt{h_{01}h_{11}(v_{11}^2-1)}}$ and $\delta_{TM_{01}\to TE_{11}} = \frac{l}{2R}\frac{k\bar{h}}{\sqrt{h_E h_H(v_{11}^2-1)}}$

where $v_{11} = 1.842$ and $v_{01} = 3.8317$.

The 15% contribution of the TM_{11} mode can be added directly in a corrugated horn antenna [72]. However, the design of the power combiner with a Gaussian wave beam output radiation can be simplified taking into account the fact that radiation of the TE_{11} mode from a smooth long conical antenna or directly from the waveguide with circular aperture comprises an insignificant part of radiated power in side lobes [73]. Therefore, with only TE_{11} radiation, since the side lobe level is negligible, this mode can be considered a good approximation of a Gaussian output. The TE_{11} loss is very small in THz and therefore still TE_{11} mode is still a reasonable option for being used in "THz gap". The reason is that TE_{11} mode is the lowest mode which is propagating in an oversize waveguide. The TE_{11} can be modeled as two plane waves traveling obliquely in the $\perp$, $\parallel$ and $-\perp$, $\parallel$ directions according to waveguide wall with angle θ each plane makes with parallel axis. $k\sin\theta = k_\perp$ and $k\cos\theta = \beta_z = k_\parallel$ (propagation constant inside waveguide). Since TE_{11} is lowest propagating in oversized waveguide, θ is small value and therefore $k_\perp$ is very small. The perpendicular component of k is responsible for conductor losses, and thus it can be concluded that TE_{11} losses is very small and can be ignored [70].

The power combining efficiency of the proposed power combiner is high so that, in most cases, very little power goes into the TM_{02} mode for the case of radial excitation or the TE_{02} mode for the case of azimuthal excitation. However, decreasing the output radius gradually can help in removing those parasitic modes from propagating. Obviously this approach does not change the power combiner's performance or efficiency and only helps to remove parasitic modes from propagating.

5.6.1 Phase Error in the Inputs

It is clear that having absolutely identical cophased inputs may not be achievable in experiment. There always is a $\Delta\varphi$ phase difference between the inputs in practice. This section is dedicated to investigating the phase tolerance effect on the output efficiency. The input rectangular waveguides are WR-2 made from PEC material in order to study just the phase tolerance effect. The inputs are excited radially and, therefore, the output dominant mode is TE_{01}.

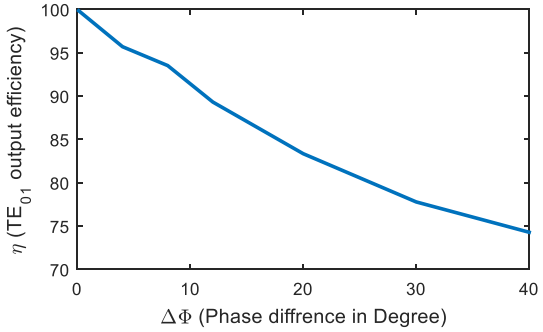

Figure 5-8 Efficiency drop as a function of phase tolerance.

The simulation study is performed by setting 6 of the waveguide input phases to $\Delta\varphi^{\circ}$ and the remaining 6 input phases to 0°. The 6 inputs with the same phase are assigned randomly without any pattern. Therefore, the drop in efficiency shows the worst case scenario.

Figure 5-8 shows how output efficiency drops as a function of Δφ of the inputs. It can be inferred, even in the case that $\Delta\varphi = 40^{\circ}$, that an output efficiency of 75% is achieved, which is still good.

5.6.2 Waveguide Overlap

The more uniform that the input power distribution to the coaxial input is, the more efficient is the mode conversion and the greater is the power combining. This Subsection studies the effect of overlapping adjacent waveguide inputs on the output power combining efficiency. At the entrance of the rectangular waveguide in the coaxial structure, a decrease in the circular waveguide radius by 5% results in overlap of the input signals Figure 5-9. shows how the overlap will lead to a more uniform input distribution and Table 5-4 compares the efficiency for two cases with $N = 12$ and for the same waveguide dimension (WR-2) as in the previous Subsection. The waveguide is made from PEC material, so THz losses are ignored in order to study the effect of overlapping. According to Table 4, a more uniform input distribution results in greater power coupling to the preferred TM_{01} output mode.

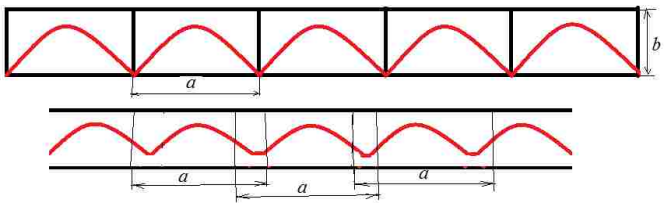

Figure 5-9 Overlap of the radial inputs and its effect on obtaining a more uniform input distribution.

Table 5-4. The ratio of output powers to input, maximum output power efficiencies and corresponding frequencies for non-overlapped and overlapped waveguides.

Excitation	$\frac{P_{TM_{01}}}{P_{TE_{10}}}$	$\eta_{TM_{01}}$	f **(GHz)**
Non-Overlapped	10.42 dB = 11.56	92%	350
Overlapped	10.79 dB = 12	100%	500

5.7 Conclusions

A power combiner to combine the output of N vacuum electron sources generating power in the THz range (0.35-0.45 THz) was propsoed. This power combiner not only combines the THz power, but also outputs a Gaussian wave beam when a TE_{10} mode is used as the input signal for each of the inputs. First results were presented for a structure operating in THz-band, which showed that for both azimuthal and radial TE_{10} mode input, the power transmission efficiency was greater than 90%. Simulations of the power combiner with realistic losses for copper show a maximum efficiency of 89%. The effects of phase errors in the input signals and the effect of waveguide overlap were also studied.

This work can lead to a simple and inexpensive solution to achieving high power output in the THz frequency range.

6 Conclusion and Future Work

In this dissertation, we discussed how group theory can be used to design a metamaterial with desired constitutive EM properties. Group theory was applied to design an all-metallic metamaterial that can survive high power microwave environments.

Based on the metamaterial design, the design of a novel multi-beam metamaterial-based backward wave oscillator is described. The idea of having a multibeam-BWO is proposed and explained for the first time here. The designed metamaterial generated 105 MW output power, which is higher than the output power of BWOs that have previously been reported in literature.

Also an innovative power combiner for THz applications, has been proposed. The power combiner adds the output of N vacuum electron sources generating power in the THz range (0.35-0.45 THz). This power combiner output mode is in the form of a Gaussian wave beam. The proposed power combiner can be scaled to the S band application and be used in combination with an MTM-BWO as a splitter. Therefore, the output power of the designed BWO can be divided in to a miimum of twelve outputs to excite twelve devices.

Future work should focus on studying the multi-beam BWO physics and try to explain the theory. Also, the designed multi-beam BWO should be built and tested using the SINUS-6 electron beam accelerator to validate the predicted 105 MW output power. Finally, the proposed structure should be tested for breakdown vulnerability.

7 References

[1] J. B. Pendry, D. Schurig and D. R. Smith, "Controlling Electromagnetic Fields," *Science,* vol. 312, pp. 1780-1782, 2006.

[2] T. Ergin, N. Stenger, P. Brenner, J. B. Pendry and M. Wegener, "Three-Dimensional Invisibility Cloak at Optical Wavelengths," *Science,* vol. 328, pp. 337-339, 2010.

[3] J. B. Pendry, "Negative Refraction Makes a Perfect Lens," *Physical Review Letters,* vol. 85, no. 18, pp. 3966-3969, 2000.

[4] N. Fang, H. Lee, C. Sun and X. Zhang, "Sub-Diffraction-Limited Optical Imaging with a Silver Superlens," *Science,* vol. 308, pp. 534-537, 2005.

[5] A. Grbic and G. V. Eleftheriades, "Overcoming the Diffraction Limit with a Planar Left-Handed Transmission-Line Lens," *Physical Review Letter,* vol. 92, no. 11, pp. 1174031-1174034, 2004.

[6] H. Chen, W. J. Padilla, J. M. O. Zide, A. C. Gossard, A. J. Taylor and R. D. Averitt, "Active terahertz metamaterial devices," *Nature,* vol. 444, pp. 597-600, 2006.

[7] W. Chen, A. Totachawattana, K. Fan, J. L. Ponsetto, A. C. Strikwerda, X. Zhang, R. D.Averitt and W. J. Padilla, "Single-layer terahertz metmaterials with bulk optical constants," *Physical Review B,* vol. 85, pp. 0351121-0351126, 2012.

[8] Y. Gao, J. P. Huang, Y. M. Liu, L. Gao, K. W. Yu and X. Zhang, "Optical Negative Refraction in Ferrofluids with Magnetocontrollability," *Physical Review Letters,* vol. 104, pp. 0345011-0345014, 2010.

[9] F. Capolino, Theory and Phenomena of Metamaterials, Boca Raton, FL, US: Taylor & Francis, 2009.

[10] L. Solymar and E. Shamonina, Waves in Metamaterials, London, UK: OXFORD, 2009.

[11] X. HU, "Some studies on metamaterial transmission lines and their applications," Doctoral Thesis in Electromagnetic Theory, KTH University, Stockholm, Sweden, 2009.

[12] R. Marques, F. Martin and M. Sorolla, Metamaterials With Negative Parameters: Theory, Design, and Microwave Applications, New York, NY: John Wiley and Sons, 2008.

[13] V. G. Veselago, "The electrodynamics of substances with simultaneously negative values of eta and mu," *Soviet Physics Uspekhi,* vol. 10, no. 4, pp. 509-514, 1967.

[14] D. R. Smith, W. J. Padilla, D. C. Vier, S. C. Nemat-Nasser and S. Schultz, "Composite Medium with Simultaneously Negative Permeability and Permittivity," *Physical Review letters,* vol. 84, no. 18, pp. 4185-4187, 2000.

[15] J.B.Pendry, A.J.Holden, W.J.Stewart and I.Youngs, "Extremely low frequency plasmons in metallic mesostructures," *Physical Review Letters,* vol. 76, no. 25, pp. 4773-4776, 1996.

[16] R. A. Shelby, D. R. Smith and S. Schultz, "Experimental Verification of a Negative Index of Refraction," *Science,* vol. 292, no. 6, pp. 77-79, 2001.

[17] J. B. Pendry, A. J. Holden, D. J. Robbins and W. J. Stewart, "Magnetism from conductors and enhanced nonlinear phenomena," *IEEE Transactions on Microwave Theory and Techniques,* vol. 47, no. 11, pp. 2075-2084, 1999.

[18] D. Schurig, J. J. Mock and D. R. Smith, "Electric-field-coupled resonators for negative permittivity metamaterials," *Applied Physics Letters,* vol. 88, pp. 0411091-0411093, 2006.

[19] R. W. Ziolkowski, "Design, Fabrication, and Testing of Double Negative Metamaterials," *IEEE Transactions on Antennas and Propagation,* vol. 51, no. 7, pp. 1516-1529, 2003.

[20] D. R. Smith, D. C. Vier, T. Koschny and a. C. M. Soukoulis, "Electromagnetic parameter retrieval from inhomogeneous metamaterials," *Physical Review E,* vol. 71, pp. 0366171- 03661711, 2005.

[21] C. A. Balanis, Electromagnetics, Advanced Engineering, United States: John Wiley & Sons, Inc., 2012.

[22] D. R. Smith and N. Kroll, "Negative Refractive Index in Left-Handed Materials," *Physical Review Letters,* vol. 85, no. 14, pp. 2933-2936, 2000.

[23] L. D. Landau and E. M. Lifshitz, Electrodynamics of Continuous Media, Oxford: Pergamon Press, 1960.

[24] Z. Szabó, G.-H. Park, R. Hedge and E.-P. Li, "A Unique Extraction of Metamaterial Parameters Based on Kramers–Kronig Relationship," *IEEE Transactions on Microwave Theory and Techniques,* vol. 58, no. 10, pp. 2646-2653, 2010.

[25] U. C. Hasar, J. J. Barroso, C. Sabah, Y. Kaya and M. Ertugrul, "Stepwise technique for accurate and unique retrieval of electromagnetic properties of bianisotropic metamaterials," *Optical Society of America,* vol. 30, no. 4, pp. 1058-1068, 2013.

[26] M. Melanie, An Introduction to Genetic Algorithms, London, England: Cambridge, Massachusetts, 1996.

[27] S. H. Gold and G. S. Nusinovich, "Review of high-power microwave source research," *Review of Scientific Instruments,* vol. 68, no. 11, pp. 3945-3974, 1997.

[28] V. L. Ginzburg, "Radiation by uniformly moving sources (Vavilov–Cherenkov effect, transition radiation, and other phenomena)," *Physics _ Uspekhi, Russian Academy of Sciences,* vol. 39, no. 10, pp. 973-982, 1996.

[29] R. B. Miller, An Introduction to The Physics of Intense Charged Particle Beams, New York, US: Plenum Press, 1985.

[30] A. Grbic and G. V. Eleftheriades, "Experimental verification of backward-wave radiation from a negative refractive index metamaterial," *Journal of Applied Physics,* vol. 92, no. 10, pp. 5930-5935, 2002.

[31] L. Schachter, Beam-Wave Interaction in Periodic and Quasi-Periodic Structures, New York: Springer, 2011.

[32] R. Kompfner, The Invention of the Travelling-Wave Tube, San Francisco, CA: San Francisco Press, 1964.

[33] J. R. Pierce, Travelling Wave Tubes, New York: Van Nostrand, 1950.

[34] S. E. Tsimring, Electron Beams And Microwave Vacuum Eelectronics, Hoboken, New Jersey: John Wiley & Sons, Inc., , 2007.

[35] A. M. N. Elfrgani, "Relativistic Backward Wave Oscillator With Gausian Radiation Pattern And Related Technologies," University of New Mexico, Albuquerque, 2015.

[36] J. S. Hummelt, "High Power Microwave Generation Using an Active Metamaterial Powered by an Electron Beam," Massachusetts Institute of Technology, Massachusetts US, 2015.

[37] C. P. STUDIO, "https://www.cst.com/," CST Computer Simulation Technology, 2017. [Online]. Available: https://www.cst.com/.

[38] L. Brillouin, Wave Propagation of Periodic Structures, New York, NY: McGraw-Hill, 1946.

[39] R. A. Silin and V. P. Sazonov, Slow-wave Structures, Boston, MA: National Lending Library for Science and Technology, 1971.

[40] A. S. Gilmour, Klystrons, Traveling Wave Tubes, Magnetrons, Cross-Field Amplifiers, and Gyrotrons, Norwood, MA: Artech House, 2011.

[41] L. J. a. R. M. J. D. Baena, "symmetry, Towards a systematic design of isotropic bulk magnetic metamaterials using the cubic point groups of symmetry," *PHYSICAL REVIEW*, vol. B 76, p. 245115, 2007.

[42] F. A. Cotton, Chemical Applications of Group Theory, 3rd ed., New York: John Wiley & Sons, 1990.

[43] M. D. B. Daniel C. Harris, Symmetry and Spectroscopy: An Introduction to Vibrational and Electronic Spectroscopy, Mineola, NY: Dover Publications Inc, 1989.

[44] S. F. A. Kettle, Symmetry and Structures, New York: John Wiley & Sons, 1985.

[45] C. M. Reinke, T. M. De la Mata Luque, M. F. Su, M. B. Sinclair and I. El-Kady, "Group-theory approach to tailored electromagnetic properties of metamaterials: An inverse-problem solution," *PHYSICAL REVIEW E,* vol. 83, no. 066603, 2011.

[46] D. G. Dudley, Mathematical Foundations for Electromagnetic Theory, Tucson: WILEY INTERSCIENCE, 1994.

[47] L. Zhang, T. Koschny and C. M. Soukoulis, "Creating double negative index materials using the Babinet principle with one metasurface," *PHYSICAL REVIEW*, vol. B 87, no. 045101, 2013.

[48] W. J. Padilla, "Group theoretical description of artificial electromagnetic metamaterials," *OPTICS EXPRESS* , vol. 15, p. 19, 2007 .

[49] S. C. Yurt, A. Elfrgani, M. I. Fuk, K. Ilyenko and E. Schamiloglu, "Similarity of properties of metamaterial slow-wave structures and metallic periodic structures," *IEEE Transactions on Plasma Sciences,* vol. 44, no. 8, pp. 1280-1286, 2016.

[50] X. Tang, Z. Duan, X. Shi, Y. Zhang and Z. Wang, "Sheet Electron Beam Transport in a Metamaterial-loaded Waveguide Under the Uniform Magnetic Focusing," *IEEE Transactions on Electron Devices,* vol. 63, no. 5, pp. 2132-2138, 2016.

[51] Z. Duan, B.-I. Wu, J. Lu, J. A. Kong and M. Chen, "Cherenkov radiation in anisotropic double-negative metamaterials," *Optics Express,* vol. 16, no. 22, pp. 18479-18484, 2008.

[52] Z. Duan, J. S. Hummelt, M. A. Shapiro and R. J. Temkin, "Sub-wavelength waveguide loaded by a complementary electric metamaterial for vacuum electron devices," *Physics of Plasmas (AIP),* vol. 21, no. 10, p. 103301, 2014.

[53] J. S. Hummelt, S. M. Lewis, M. A. Shapiro and R. J. Temkin, "Design of a Metamaterial-Based Backward-Wave Oscillator," *IEEE Transactions on Plasma Sciences,* vol. 42, no. 4, pp. 930-936, 2014.

[54] Y. P. Bliokh, S. Savel'ev and F. Nori, "Electron-Beam Instability in Left-Handed Media," *Physical Review Letters,* vol. 100, p. 244803, 2008.

[55] M. A. Shapiro, 1. S. Trendafilov, Y. Urzhumov, 3. A. Alu, R. J. Temkin and G. Shvets, "Active negative-index metamaterial powered by an electron beam," *Physical Review B,* vol. 86, p. 085132, 2012.

[56] D. M. French, D. Shiffler and K. Cartwright, "Electron beam coupling to a metamaterial structure," *Physics of Plasmas,* vol. 20, p. 083116, 2013.

[57] Y. Wang, Z. Duan, F. Wang, S. Li, Y. Nie, Y. Gong and J. Feng, "S-Band High-Efficiency Metamaterial Microwave Sources," *IEEE Transactions on Electron Devices,* vol. 63, no. 9, pp. 3747-3752, 2016.

[58] S. C. Yurt, M. I. Fuks, S. Prasad and E. Schamiloglu, "Design of a metamaterial slow wave structure for an O-type high power microwave generator," *Physics of Plasmas,* vol. 23, p. 123115, 2016.

[59] M. I. Fuks, "Forming of Relativistic Electron Beam in Coaxial Diode with Magnetic," *Sov. Phys. Tech,* vol. 27, no. 4, pp. 451-453, 1982.

[60] C. Baker, W. R. Tribe, T. Lo, B. E. Cole, S. Chandler and M. C. Kemp, "People Screening using Terahertz Technology," *SPIE Proceedings, Terahertz Science and Applications,* vol. 5790, pp. 1-10, June 22nd, 2005.

[61] R. A. Lewis, "A review of terahertz sources," *Journal of Physics D Applied Physics*, vol. 47, pp. 3740011-37400111 , 2014.

[62] B. A. Knyazev, G. N. Kulipanov and N. A. Vinokurov, "Novosibirsk terahertz free electron laser: instrumentation development and experimental achievements," *Measurement Science and Technology, IOP Science,* vol. 21, pp. 0540171-05401713 , 2010.

[63] M. Glyavin, G. Denisov, V. Zapevalov, A. Kuftin, A. Luchinin, V. Manuilov, M. Morozkin, A. Sedov and A. Chirkov, "Terahertz Gyrotrons: State of the Art and Prospects," *Journal of Communications Technology and Electronics,* vol. 59, p. 792–797, 2014.

[64] B. J., J. Swegle and E. Schamiloglu, High Power Microwaves, Boca Raton, FL: CRC Press, 2016.

[65] A. El'chaninov, A. Klimov, O. Koval'chuk, G. Mesyats, I.V.Pegel, I. Romanchenko, V. Rostov, K. Sharypov and M. Yalandin, "Coherent Summation of Power of Nanosecond Relativistic Microwave Oscillators," *Technical Physics,* vol. 56, no. 1, pp. 121-126, 2011.

[66] V. V. Rostov, A. A. Elchaninov, I. V. Romanchenko and M. I. Yalandin, "A coherent two-channel source of Cherenkov superradiance pulses," *Applied Physics Letters (AIP),* vol. 100, pp. 2241021-22410214, 2012.

[67] M. I. Yalandi, S. A. Shunailov, M. R. Ul'maskulov, K. A. Sharypov, V. G. Shpak, V. V. Rostov, I. V. Romanchenko, A. A. El'chaninov and A. I. Klimov, "Synphase operation of nanosecond relativistic 37-GHz backward-wave oscillators without

electrodynamic coupling," *Technical Physics Letters,* vol. 38, no. 10, p. 917–920, 2012.

[68] Q. Xue, K. Song and C. H. Chan, "China: Power Combiners/Dividers," *IEEE Microwave Magazine,* vol. 5, pp. 96-106, May 2011.

[69] N. Ginzburg, A. Cross, A. Golovanov, G. Mesyats, M. Pedos, A. Phelps, I. Romanchenko, V. Rostov, S. Rukin, S. K. A., S. V. G, M. Shunailov, Ulmaskulov, M. Yalandin and I. Zotova, "Generation of electromagnetic fields of extremely high intensity by coherent summation of Cherenkov superradiance pulses," *Physical Review Letters (PRL),* vol. 115, pp. 1148021-1148025 , 2015.

[70] D. M. Pozar, Microwave Engineering, 4th Edition, Hoboken, New Jersey: John Wiley & Sons, 2012.

[71] B. Katsenelenbaum, L. M. D. Rio, M. Pereyaslavets, M. S. A. and M. T. , Theory of Nonuniform Waveguides: The Cross-Section Method, Edison, NJ: The Institution of Engineering and Technology, 1998.

[72] E. Abubakirov, M. Fuchs and N. Kovalev, "High-selectivity resonator for powerful microwave sources," in *11th International Conference on High-Power Particle Beams,* Prague, Czech Republic, 1996.

[73] Y. Lo and S. Lee, Antenna Handbook: Antenna theory, New York, NY: Springer, 1994.

[74] B. N. Breizman and D. D. Ryutov, "Powerful Relativistic Electron Beam in a Plasma and in a Vacuum (Theory)," *Nuclear Fusion,* vol. 14, pp. 873-907, 1974.

[75] J. Domingo Baena, J. Bonache, F. Martín and R. Marqués Sillero, "Equivalent-Circuit Models for Split-Ring Resonators and Complementary Split-Ring Resonators Coupled to Planar Transmission Lines," *IEEE TRANSACTIONS ON MICROWAVE THEORY AND TECHNIQUES*, vol. 53, no. 4, APRIL 2005.

[76] M. Durán-Sindreu, J. Naqui, F. Paredes, J. Bonache and F. Martín, "Electrically Small Resonators for Planar Metamaterial, Microwave Circuit and Antenna Design: A Comparative Analysis," *applied sciences*, vol. 2, pp. 375-395, 2012.

[77] "Equivalent-Circuit Models for Split-Ring Resonators and Complementary Split-Ring Resonators Coupled to Planar Transmission Lines".